Multistage hydration during oceanic serpentinisation revealed by in situ oxygen isotope and trace element analyses

Coralie Vesin, Daniela Rubatto, Thomas Pettke, Etienne Deloule

Geochimica et Cosmochimica Acta 355 (2023) 13–31

Contents lists available at ScienceDirect

Geochimica et Cosmochimica Acta

journal homepage: www.elsevier.com/locate/gca

Multistage hydration during oceanic serpentinisation revealed by *in situ* oxygen isotope and trace element analyses

Coralie Vesin [a,*], Daniela Rubatto [a,b], Thomas Pettke [a], Etienne Deloule [c]

[a] Institute of Geological Sciences, University of Bern, Bern CH-3012, Switzerland
[b] Institut des Sciences de la Terre, University of Lausanne, Lausanne CH-1015, Switzerland
[c] Université de Lorraine, CNRS, CRPG, F-54000 Nancy, France

ARTICLE INFO

Associate editor: Frieder Klein and Jeffrey G. Catalano

Keywords:
Oceanic serpentinisation
Serpentine textures
Oxygen isotopes
Fluid-mobile elements
Transition metals

ABSTRACT

Serpentinisation of mantle peridotites below the seafloor is the most important hydration reaction in the Earth's deep water cycle. This critical step in water–rock interaction occurs over multiple serpentinisation stages and at variable temperatures and fluid compositions. We present the first study using spatially coupled in-situ analysis of oxygen isotopes (secondary ionization mass spectrometry) and trace elements (laser ablation inductively coupled plasma mass spectrometry) to unravel the multistage hydration history of oceanic serpentinites. We study samples from the Newfoundland-Iberia extended passive margins, which represents a magma-poor ocean-continent transition zone (Ocean Drilling Program cores, Leg 173 Site 1070 from Iberia, Leg 210 Site 1277 from Newfoundland). The concentrations of the fluid mobile elements chlorine and boron in serpentine are used as a proxy for the salinity of the serpentinising fluid. The correlation of Cl/B with $\delta^{18}O_{serpentine}$ compositions provides new insights to disentangle temperature from fluid composition effects. The transition metal composition (V, Co, Sc, Mn, Zn, Ni, Cr) of dominantly lizardite in mesh after olivine and in bastite after orthopyroxene shows a chemical redistribution between textural sites in the Newfoundland samples, indicating the simultaneous serpentinisation of olivine and orthopyroxene. This feature is not observed in the Iberian samples, for which we propose sequential reactions. Lizardite in samples from both localities varies considerably in oxygen isotope composition at the scale of tens of micrometres depending on texture, with a range in $\delta^{18}O$ of 3.3–13.5‰ for Iberia samples and a more restricted range of 5.7–9.3‰ for Newfoundland samples. Temperatures calculated from the $\delta^{18}O_{serpentine}$ corresponding to the lowest Cl/B ratio (interpreted as closest to seawater composition) indicate sequential serpentinisation with decreasing temperature from ~190 to ~60 °C in the Iberia setting. The Newfoundland samples were serpentinised at a lower temperature (100–130 °C), possibly at a shallower depth. Serpentinisation in the Newfoundland samples probably produced a concentrated amount of H_2 in a shorter period of time, whereas in the Iberian samples a small but prolonged amount of H_2 was produced, possibly creating more favourable conditions for microbial activity.

1. Introduction

Aqueous fluid in the solid Earth is involved in a number of fundamental processes, from the rheological and seismic behaviour of the lithosphere, to the formation of volcanic arcs and, ultimately, new continental crust. Serpentinisation of mantle-derived ultramafic rocks is the dominant process that transfers water from the hydrosphere to the lithosphere. Mantle peridotite is hydrated by interaction with ocean water when exposed at mid-ocean ridges (e.g., Francheteau et al., 1990; Mevel and Stamoudi, 1996; Bach et al., 2006), ocean transform faults and extended passive margins (e.g., Agrinier et al., 1988; Beard and Hopkinson, 2000; Skelton and Valley, 2000) where seawater can penetrate deep into the lithospheric mantle along kilometre-scale faults. The chemical reaction during oceanic serpentinisation oxidises Fe, producing H_2, CH_4 and other organic compounds that may have played key role in the first appearance of life on Earth (e.g., Sojo et al., 2016; Brovarone et al., 2020; Liu et al., 2023). Despite the importance of the serpentinisation processes, the systematics of water uptake during hydration is poorly understood in terms of hydration sequence and chemical exchanges.

The different settings in which hydration of oceanic lithosphere can occur result in variable conditions of serpentinisation, with

* Corresponding author.
E-mail address: coralie.vesin@unibe.ch (C. Vesin).

https://doi.org/10.1016/j.gca.2023.06.032
Received 26 January 2023; Accepted 27 June 2023
Available online 29 June 2023

temperatures ranging from near zero to above ~400 °C (e.g., Bowen and Tuttle, 1949). Moreover, the fluid involved in the hydration starts as pure seawater but can become "hydrothermally-evolved" seawater through interaction with crustal and mantle rocks (e.g., Campbell et al., 1988). The resulting oceanic serpentinites are thus compositionally variable on scales ranging from regional geotectonic setting (e.g., mid-ocean ridges, convergent and passive margins) to micrometre-scale rock textures (e.g., Agrinier et al., 1988; Francheteau et al., 1990; Scambelluri et al., 2001; Kodolányi et al., 2012; Deschamps et al., 2013; Rouméjon et al., 2015).

Water does not serpentinise peridotites uniformly, but rather the mantle minerals break down according to different reactions and possibly in distinct stages. While at lower temperature olivine is the first phase to serpentinise, high temperature may favour pyroxene serpentinisation (e.g., Martin and Fyfe, 1970). Olivine is destabilised by the fluid following the reaction (Evans, 2008):

$$\text{Mg-Fe-Olivine} + H_2O = \text{Mg-Fe-Serpentine} + \text{Mg-Fe-Brucite} \pm \text{Magnetite} \quad (1)$$

The products form a mesh texture around the unreacted olivine and eventually replace olivine completely. Orthopyroxene is commonly affected by serpentinisation with subsequent hydration, with the fluid infiltrating the cleavages and proceeding towards the grain interior (Prichard, 1979). The relevant simplified reaction is (modified from Bach et al., 2006):

$$\text{Orthopyroxene} + H_2O = \text{Serpentine} + SiO_2\ (aq) \pm \text{Magnetite} \quad (2)$$

This pseudomorphic replacement of orthopyroxene by serpentine is called "bastite", and the excess SiO_2(aq) would either be accommodated by the crystallisation of talc in case of a close-system (Klein and Le Roux, 2020) or lost with the fluid in an open-system. A coupled reaction of olivine and orthopyroxene has been proposed by Evans (2004), here simplified as:

$$\text{Olivine} + \text{Orthopyroxene} + H_2O = \text{Serpentine} + \text{Magnetite} + H_2 \pm \text{Brucite} \pm \text{Talc} \quad (3)$$

Depending on bulk rock SiO_2 contents, in particular the olivine/orthopyroxene ratio, brucite (e.g., Bach et al., 2006; Kodolányi et al., 2012; Klein et al., 2013, 2020) or talc (in the case of metasomatic SiO_2 addition) may form in addition. Magnetite and carbonate crystallisation depends on the modes of the primary mantle minerals (e.g., Frost and Beard, 2007), the temperature (e.g., Klein et al., 2014) and the composition of the serpentinising fluid (e.g., Schwarzenbach et al., 2013). Overall, these reactions not only result in complex microtextures, but can also produce diverse mineral trace element and isotopic compositions, due to the variable conditions of serpentinisation such as temperature, redox conditions, water–rock ratio and fluid composition (e.g., Bach et al., 2004; Kodolányi et al., 2012). To unravel this complexity and gain an understanding of the conditions and element transfer during serpentinisation, the coupled investigation of trace elements and isotopic signatures of individual serpentine textures needs to be approached with *in situ* analysis.

The investigation of trace element compositions of the serpentine can provide insights on the protolith and fluid composition. Fluid-immobile elements are not influenced by fluid interaction (e.g., Niu, 2004; Deschamps et al., 2010) and thus their concentrations in the reaction product (i.e., serpentine) are interpreted to reflect the primary minerals (i.e., olivine and orthopyroxene) and hence the protolith composition (e.g., Deschamps et al., 2013; Rouméjon et al., 2019). Conversely, fluid-mobile elements (FME, e.g., Cl, B, Li, Sr, As, Sb, Cs) are dominantly sourced from the fluid and their concentration in serpentine tracks the fluid composition (e.g., Kodolányi et al., 2012).

The bulk composition of oceanic serpentinites show significant enrichments for some specific FME. Trace element patterns of serpentinites from different geotectonic settings of oceanic serpentinisation show variable enrichments in Li, B, Na, K, Cl, Rb, Sr, Cs, Ba, As, Sb and W (e.g., Niu, 2004; Paulick et al., 2006; Kodolányi et al., 2012; Peters et al., 2017). Similar enrichments have been found in orogenic antigorite-serpentinites from Erro-Tobbio (Italy) and were interpreted as the result of ocean floor serpentinisation (Scambelluri et al., 1995; Peters et al., 2017). It has been shown that oceanic serpentinised ultramafic rocks contain in the order of 0.05–1 wt% Cl, found either as structurally bound Cl or as water-soluble chlorides (e.g., Barnes and Sharp, 2006; Kodolányi et al., 2012; Kendrick et al., 2013). *In situ* data of serpentine crystallising in distinct textures of mid-ocean ridge serpentinites have revealed that serpentine in mesh texture is more Cl-rich than serpentine in bastite texture (Agrinier et al., 1988; Früh-Green et al., 1996; Mevel and Stamoudi, 1996). Boron concentrations also vary between texture in mid-ocean ridge serpentinites from B-poor in mesh to B-rich in bastite, and Li shows the same trend (Kodolányi et al., 2012). The trace element behaviour during the transition from lizardite/chrysotile to antigorite has been investigated by Kodolányi and Pettke (2011), who have shown that up to 90% of Cl, 80% of B and 50% of Sr are lost in the fluid during the transition, demonstrating that antigorite has a lower affinity for FME uptake. Similar conclusions were drawn by Rouméjon et al. (2019) for the Atlantis Massif and the South Indian Ridge, where antigorite is Mn- and Sn-enriched, but depleted in seawater-derived FME. Serpentinites formed in forearc (e.g., Mariana forearc) and subduction zone environments are significant enriched in Li, Sr, Rb, Cs, Ba and As, sourced from sediment dehydration in the subducting slab (Kodolányi et al., 2012; Deschamps et al., 2013; Kahl et al., 2015; Albers et al., 2020).

The oxygen isotopic composition of oceanic serpentinites reflects the serpentinisation environment. The fractionation factor between water and serpentine depends on temperature (Wenner and Taylor, 1971, 1973). Numerous studies have reported oxygen isotope compositions of oceanic serpentinites for bulk rock samples (e.g., Agrinier et al., 1988; Skelton and Valley, 2000; Alt et al., 2007), for mineral separates without textural differentiation (Agrinier et al., 1995, 1996; Früh-Green et al., 1996; Barnes et al., 2009), and for mineral separates with textural distinction (mesh, bastite or vein; Agrinier and Cannat, 1997). The heavy oxygen isotope signatures of serpentine from the Iberia passive margin have been interpreted to indicate low-temperature serpentinisation (Agrinier et al., 1988, 1996; Skelton and Valley, 2000). Serpentinites from the Southwest Indian Ridge show oxygen isotope compositions lower than the mantle signature ($\delta^{18}O = 5.5 \pm 0.5‰$, Mattey et al., 1994), usually interpreted as a the result of high-temperature serpentinisation (Decitre et al., 2002). Similar ranges have been measured on serpentine mineral separates from drill core from the Mid-Atlantic Ridge Kane Fracture Zone, displaying a variation of 2–3‰ for a given drill site (Wenner and Taylor, 1973; Agrinier and Cannat, 1997). Bulk rock compositions of serpentinised peridotites from numerous Mid-Atlantic Ridge drill cores worldwide returned heavier oxygen isotope compositions (Alt et al., 2007) compared to the composition of serpentine minerals in the same drill site (Barnes et al., 2009). The difference between the bulk and mineral measurements can be caused by the presence of possible mantle mineral relicts and crystallisation of additional phases during the serpentinisation reaction. In all cases, the measurements represent average signatures of the sample or serpentine separate. Even where textural differentiation has been considered, bulk sampling methods cannot resolve possible heterogeneities at the tens of micrometre scale between textural sites in a given sample. To mitigate this problem, oxygen isotope serpentine standards have recently been developed (Scicchitano et al., 2018), allowing accurate *in situ* analysis by secondary ion mass spectrometry (SIMS).

This study investigates serpentinised samples from the extended passive margins of Iberia and Newfoundland. This setting is a typical example of an ocean-continent transition zone (OCT), i.e., the continuous transition from the thinned passive continental margin to the oceanic lithosphere (e.g., Whitmarsh and Sawyer, 1996). We present *in situ* analyses of serpentine in different textural sites (mesh, bastite and veins) and the chemical characterisation of major, minor and trace elements, coupled to oxygen isotopes. While transition metals are used to

detect any chemical redistribution between textural sites, the spatial correlation of Cl/B (a proxy for fluid salinity) and O isotopic compositions of serpentine provides new insights to disentangle the effect of temperature and fluid composition during serpentinisation reactions. Our findings not only emphasise the importance of *in situ* measurements, but also provide strong evidence for multistage water incorporation in the ultramafic rocks with varying serpentinisation conditions within a single setting.

2. Geological setting

This study investigates samples from the extended passive margins retrieved by drill cores of Ocean Drilling Program (ODP) Leg 173 Site 1070 from Iberia and Leg 210 Site 1277 from Newfoundland (Fig. S1). Numerous studies have highlighted the subcontinental nature of the lithospheric mantle (Abe, 2001; Hébert et al., 2001), overlain by mid-ocean ridge basalts in some drill cores (Robertson, 2007). The Iberia-Newfoundland conjugate margins have been interpreted as a typical example of a magma-poor interface between the advanced stage of rifting and the onset of slow seafloor spreading (e.g., Whitmarsh and Sawyer, 1996). The Iberia and Newfoundland passive margins are a conjugate non-volcanic rift system (e.g., Reid, 1994) that includes a complex suite of different extensional modes (Péron-Pinvidic and Manatschal, 2009). Initial thinning of the crust resulted from localised stretching (<10 km) with uncoupled faults acting as a conjugate detachment fault system. Progressive rifting induced exhumation of mantle rocks by basement detachment faults cutting through the crust into the mantle. The establishment of the embryonic, slow-spreading ocean ridge at 115 Ma (Eddy et al., 2017) acted as a localised thermal and mechanical driver for seafloor spreading. The Iberia margin represents a classic OCT with exposed serpentinised peridotite basement. This peridotite ridge is discontinuous, suggesting that each segment corresponds to a spreading step during the continental break-up (Beslier et al., 1993). On the other hand, the oceanic basement of the Newfoundland margin is thought to have been produced by the coaction of extension and magmatism, after a shift from extensional mode during non-volcanic rifting (i.e., exhuming serpentinised mantle), to magma-poor volcanism during oceanic crust emplacement (Shillington et al., 2006).

The lowermost part of the drillcore from Site 1070, Iberia Passive Margin (Fig. S1) is partly composed of massive serpentinised peridotite including both harzburgite and lherzolite (Whitmarsh et al., 1998).

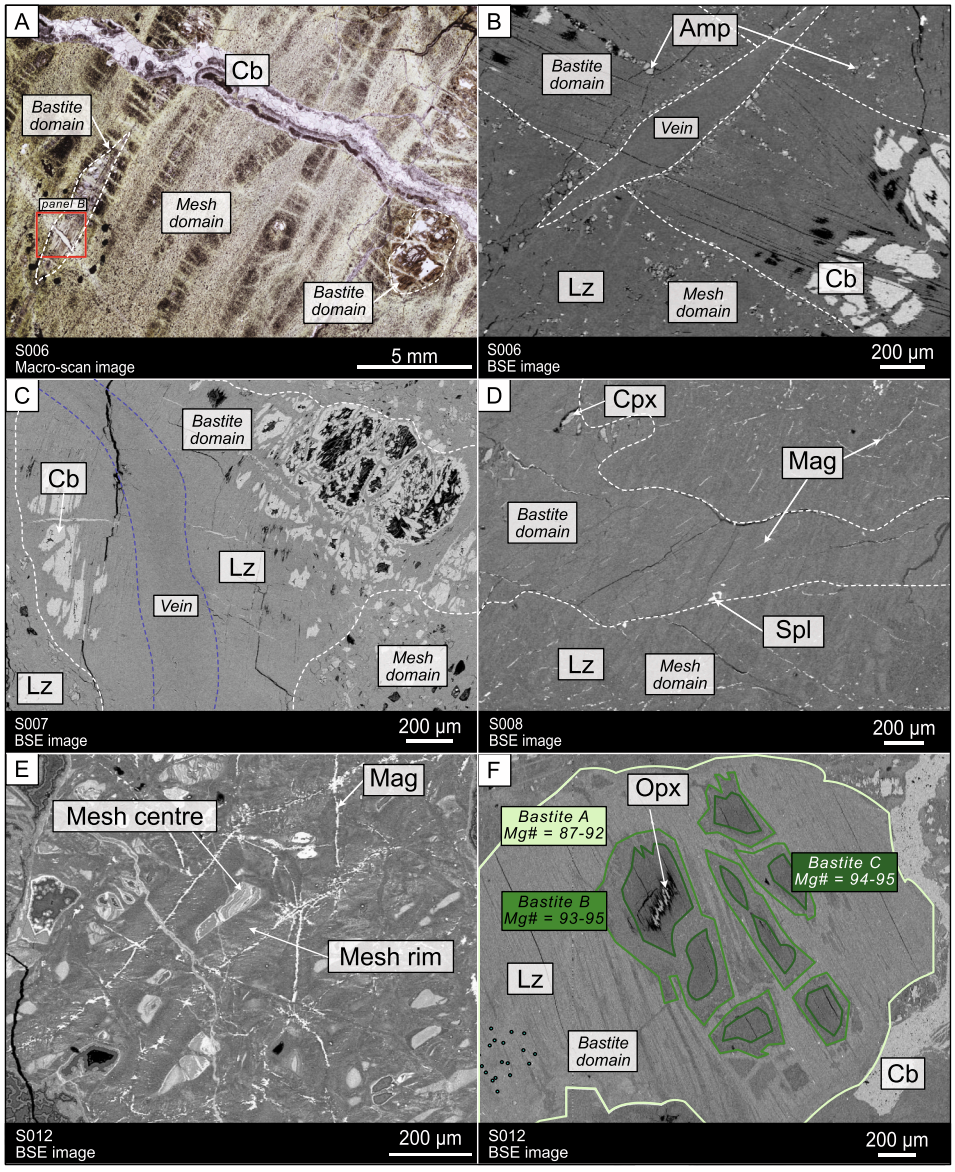

Fig. 1. Serpentine textures on the site of primary olivine and orthopyroxene. Mineral abbreviations are from Whitney and Evans (2010). (A) Transmitted light image of mesh in sample S006 (Newfoundland) with minor bastite (white dashed line) and a late, undeformed carbonate (Cb) vein crosscutting both domains. The stretched pattern of the rock has been attributed to ductile deformation prior to mantle exhumation (Tucholke et al., 2004). (B) BSE image of a close-up of (A) where a serpentine vein crosscuts bastite and mesh. Carbonates replace the initial mantle orthopyroxene as a late feature. Amphibole (Amp) is found as small crystals (<10 µm) in the mesh and the bastite domains. The black zones in the bastite are holes formed during sample preparation. (C) BSE image of sample S007 (Newfoundland). The bastite domain is mainly composed of lizardite (Lz) with minor carbonate. A lizardite veincutting the bastite is highlighted by the blue dashed-line. The black zones in the bastite are holes formed during sample preparation. (D) BSE image of both mesh and bastite domains in sample S008 (Iberia). Magnetite (Mag) forms along bastite cleavage and mesh rims. Minor clinopyroxene (Cpx; diopside) remnants are preserved in the bastite domain. (E) BSE image of a mesh domain with distinct mesh rim and centres (S012, Iberia). Magnetite forms along the mesh network. (F) BSE image of a bastite grain from sample S012. The chemical zones have distinct Mg# and are marked by the green lines. A remnant of mantle orthopyroxene is present in the centre of bastite C. A carbonate vein is present to the right of the bastite.

Gabbro pegmatite dykelets and pyroxenites crosscut the peridotite in places. The upper part of the serpentinised peridotite section is slightly foliated and overlain by a 3 m-thick pegmatitic gabbro unit. This rock unit is covered by tectonite-breccia composed of serpentinised peridotite and gabbro clasts. Up to 650 m of fine-grained sediments (claystone to siltstone) make up the uppermost part of the core. The samples from this site have been renamed and characterised in detail by Kodolányi et al. (2012): for our study, we selected the least serpentinised and deformed samples, S008 and S012 (Table S1; see Fig. S2 for the macroscopic scans of the thin sections).

The core from Site 1277A (Fig. S1) on the Newfoundland passive margin recovered approximately 40 m of serpentinised harzburgite at the bottom of the core, which is variably mylonitised (Tucholke et al., 2004). The stretched pattern of the serpentinised mantle rocks (Fig. 1A) results from a ductile deformation prior to the mantle exhumation stage (Tucholke et al., 2004). Thin gabbroic dykelets crosscut the drillcore, and carbonate veinlets are present in some parts. The sequence is capped by 85 m of siltstone to sandstone. Basaltic breccias to polimict tectonite-breccia and mass-flow deposits occur in between these two portions. Samples S006 and S007, also renamed and characterised in detail by Kodolányi et al. (2012), are from this site (Table S1; see Fig. S2 for the macroscopic scans of the thin sections) and represent the least deformed samples.

3. Analytical methods

Petrographic characterization of the thin sections focused on mineralogical and textural systematics and used transmitted light microscopy. The samples investigated in detail were selected based on the petrographic observation where distinct serpentine textures are visible and mixtures with co-product phases of the serpentinisation are minimal. To better illustrate textural domains in the samples, back-scattered electron (BSE) imaging was performed with a Scanning Electron Microscope (SEM, ZEISS EV050) at the Institute of Geological Sciences, University of Bern, operating at low vacuum conditions, 20 kV, a beam current of 100 μA and a working distance of ~9.5 mm. Raman spectroscopy assisted the determination of serpentine (lizardite, chrysotile or antigorite). The instrument used is a Jobin Yvon LabRAM-HR800, University of Bern, that is set up with a 532 nm green laser source, a dry 100x objective, 1000 μm hole and 100 μm slit. Every Raman session started with a calibration of the 520.6 cm^{-1} band on a Silicon wafer.

3.1. Electron probe microanalysis (EPMA)

Major and minor element concentrations of the minerals were measured with a JEOL JXA 8200 electron probe at the University of Bern, using wavelength-dispersive X-ray spectrometry (WDS). Thin sections were carbon coated and the samples were analysed with a beam diameter of 10 μm, a beam current of 5 nA, an acceleration voltage of 15 kV with an acquisition time of 20 s on the peak and 10 s on the background. Ten element oxides were calibrated using the following standards: orthoclase (SiO_2), forsterite (MgO), magnetite (FeO), anorthite (Al_2O_3, CaO), tugtupite (Cl), chromium spinel (Cr_2O_3), pyrolusite (MnO), bunsenite (NiO), rutile (TiO_2).

X-ray mapping was performed on the same instrument using wavelength-dispersive X-ray spectrometry (WDS) for Si, Al, Mg, Fe, Cl, and energy-dispersive X-ray spectrometry (EDS) for Ca, Ti, Cr, Mn, Ni. The instrument was operated with a 100 nA beam current and 15 kV acceleration voltage. The step size was 2 μm and the dwell time between 180 and 200 ms. After processing, the intensity maps were calibrated into quantitative maps with XMapTools 4 (Lanari et al., 2014, 2019), running on Matlab.

3.2. Laser ablation inductively coupled plasma mass spectrometry (LA–ICP–MS)

The trace element composition of the serpentine was measured by LA–ICP–MS at the Institute of Geological Sciences, University of Bern. The Resonetics RESOlutionSE 193 nm excimer laser system is equipped with an S-155 large volume constant geometry ablation cell, from Laurin Technic, Australia. This is coupled to an Agilent 7900 quadrupole ICP–MS system. Daily optimisation of ICP–MS conditions included tuning for low oxide production (ThO/Th ~ 0.16%) and robust plasma conditions monitored by equal sensitivity of U and Th (Th/U ~98%). For sample measurements, the beam size was 38 μm, and was limited by the size of homogeneous domains for measurement. External standardization was against GSD-1G from USGS, employing values reported in Peters and Pettke (2017), and Sca17 for Cl (Seo et al., 2011). Internal standardization used Si concentrations on minerals from the same textural position, measured by EPMA. Data reduction was performed using Iolite IgorPro, employing the limits of detection (LOD) calculation formula reported in Pettke et al. (2012). Measurement accuracy was monitored by measuring SRM612 from NIST as unknown (in absence of a serpentine mineral standard) and is better than 10% for most elements with the exception of B (18%), As (25%), Gd (16%) and Bi (20%).

3.3. Secondary Ionization Mass Spectrometry (SIMS)

The thin sections were cleaned from carbon-coating and polished again to achieve a high-quality polish with successive decreasing micrometre diamond pastes. Millimetre-sized pieces were cut from the thin sections with a diamond-wire saw and then mounted in indium rings, along with an epoxy chip containing the reference materials. The indium mounts were then sputter-coated with ~40 Å of gold.

Oxygen isotope measurements were performed on both the CAMECA 1270–E7 ion probe at CRPG-CNRS (Nancy, France) and the CAMECA IMS 1280–HR housed at the SwissSIMS laboratory, part of the Centre for Advanced Surface Analysis (CASA) platform, University of Lausanne. The ion probes were configured with a 2 nA Cs^+ primary beam at 10 kV accelerating voltage. The secondary negative ions were extracted with an accelerating voltage of 10 kV, passing through a 243 μm field aperture and with a mass resolution of 5000. The spot diameter was approximately 20 μm. The acquisition cycles started after 120 s of pre-sputtering time. The two oxygen isotopes ^{16}O and ^{18}O were acquired simultaneously on Faraday cups. The ^{16}O count rate was varying from 1.25 to 1.55 × 10^9 counts per second. The oxygen isotope compositions are referenced to the Vienna Standard Mean Ocean Water (V–SMOW) and expressed in δ notation.

The oxygen isotope measurements were calibrated against lizardite reference materials developed by Scicchitano et al. (2018): lizardite L3431 from the Mineralogical Collection of the Research School of Earth Sciences (ANU; $\delta^{18}O = 5.26 \pm 0.20‰$). The two other serpentine standards (Cerro del Almirez antigorite AL06-44A, $\delta^{18}O = 8.30 \pm 0.12‰$; and chrysotile C22908, $\delta^{18}O = 4.37 \pm 0.02‰$) were analysed along with the lizardite to investigate any instrumental mass fractionation (see below). The San Carlos Olivine (SCO, $\delta^{18}O = 5.26 \pm 0.05‰$, 1σ; Eiler et al., 1996) standard was additionally measured to monitor stability and instrumental mass fractionation. The matrix-matched standard (lizardite in all cases) was analysed every six unknowns. Individual measurements of standards and samples showed internal uncertainties in the order of 0.10–0.31‰ (2σ). The repeatability of the standard varied for each measurement session, from 0.30 to 0.50‰ (2σ) for SCO and from 0.30 to 0.63‰ for lizardite.

Lizardite L3431 has a Mg# = 98.3 (Mg# = molar Mg / [Mg + Fe_{tot}]; $Fe_{tot} = Fe^{2+}$ is used throughout because of the lack of Fe^{3+} data), which is slightly higher than the composition of our samples (Mg# ranges 87–96, with the exception of a textural site of one sample down to Mg# 75). Scicchitano et al. (2021) investigated the matrix effect on an antigorite standard and highlighted a maximum bias of ~1.8‰ for a

compositional range of Mg# = 77.5–99.5%. There is no study of the matrix effect for lizardite and chrysotile, but we estimate that any matrix effect between the lizardite standard and the unknowns would likely be within the uncertainty of the measurements. Additionally, the measured instrumental mass fractionation between the three serpentine ranges from 0.1 to 0.6‰. This latter test ensures that, if minor mixing occurred between lizardite and chrysotile, the obtained $\delta^{18}O$ values obtained are still sufficiently accurate.

3.4. Strontium isotopes measurements

Bulk sample Sr isotope ratio measurements were performed on a Thermo Scientific Triton Plus Thermal Ionization Mass Spectrometer (TIMS) at the Institute of Geological Sciences, University of Bern. Conventional HF-HNO_3 dissolution and ion exchange procedures using Sr-resin were conducted to separate strontium from the matrix for the four samples and USGS-BCR-2 standard (the standard run as an unknown to check for accurate procedures). Instrument stability was evaluated with 3 replicates of NIST-SRM987 standard throughout the collection of isotopic data, giving an average value of 0.710285 ± 2 (2σ, Table S2) slightly more radiogenic than the reference value (0.710248; Weis et al., 2006). USGS-BCR-2 run as a procedural standard returned slightly more radiogenic $^{87}Sr/^{86}Sr = 0.705036 \pm 3$, Table S2) compared to the reference value (0.705019; Weis et al., 2006). The measurement data for our samples as well as for SRM987 were normalised to the certified value for SRM987 standard. The shift between the measured USGS-BCR-2 standard and the reference value is not significant for interpretation of our samples results (Table S2).

4. Results

4.1. Petrography and textural relationships

4.1.1. Mantle minerals

Mantle olivine is no longer present in the samples, but completely replaced by serpentine mixed with other phases. The fractions of orthopyroxene remnants vary between the samples and are most abundant in S008 (Iberia, Table S1). S012 (Iberia) is clinopyroxene-rich (modes of up to 30%) and the crystals show tiny exsolution lamellae of orthopyroxene, now largely serpentinised, while clinopyroxene is well preserved. Minor chromium-rich spinel is present in samples S006, S007 (Newfoundland) and S008 (Iberia). For a more complete description of the samples see Kodolányi et al. (2012).

4.1.2. Serpentine texture

Serpentinisation of mantle olivine can form two distinct microtextures: (i) fine grained serpentine minerals with more or less magnetite along the mesh network and irregular fractures are referred to as "mesh rim" (Fig. 1E), whereas (ii) "mesh centres" indicate the serpentine that has completely replaced the rest of the olivine (Fig. 1E). These two textural domains are well developed in samples S008 and S012 from the Iberia passive margin. Raman spectroscopy indicates that lizardite is the predominant serpentine mineral crystallising in the mesh rim (Kodolányi et al., 2012; Fig. S3). The distinction of the serpentine in the mesh centre is more challenging as it is very fine-grained and can be a mixing of different hydrous phases (e.g., Raman evidence for unidentified phase in mesh centres of S012, Iberia, Fig. S3). In Newfoundland samples S006 and S007 a distinction of mesh rims and centres is not possible and thus the hydration of olivine in these samples is referred to as 'mesh' without further distinction.

The hydration of orthopyroxene resulted in the pseudomorphic crystallisation of serpentine in a bastite texture (Fig. 1A, B, C, D, F). The hydration progressed along the cleavage plains into the crystals. Partial (with visible orthopyroxene relict in the centre, Fig. 1F) to complete crystallisation of bastite is recorded by the investigated samples. Lizardite is the main polymorph comprising the bastite, but presence of intimately intergrown chrysotile at micrometre scale is suggested by Raman spectra (Kodolányi et al., 2012; Fig. S3).

Serpentine veins are observed as crosscutting features in S006 (Fig. 1A, B) and S008 (not visible by BSE images but highlighted by the chemical maps, Fig. 2D–F). In S006 (Newfoundland), the main vein is composed of lizardite (±chrysotile), is hundreds of micrometres wide and crosscuts both the mesh and the bastite. Smaller veinlets (tens of micrometres) are texturally linked to the central vein. In S008 (Iberia), veinlets of mixed lizardite and chrysotile infiltrate through mesh and bastite textures (Fig. 2D–F). Antigorite was not observed in the four samples investigated here.

The observed textural serpentine domains (i.e., mesh versus bastite) concur with the conclusion of Kodolányi et al. (2012) that the protolith of the Newfoundland samples S006, S007 and of the Iberia sample S008 is harzburgite, whereas sample S012 (Iberia) likely represents a former olivine-websterite (olivine-rich pyroxenite).

4.1.3. Other phases

Magnetite is rare, accounting for <1% of the thin-section area in all our samples (estimated with point counting by Kodolányi et al., 2012). When present, micrometre scale grains of magnetite (0.1–5 μm) are located in the mesh rim texture along with serpentine (Fig. 1D, E), in the mesh centres in S012 (Iberia, Fig. 1E), and also in bastite in sample S008 (Iberia, Fig. 1D). Brucite was not observed in optical microscopy nor in BSE images in our samples. Moreover, no specific peaks that relate to brucite in the Raman spectra are visible (see reference brucite spectrum in Fig. S3). The EPMA totals of serpentine measurements (single spot analysis and X-ray maps) are above ca. 80 wt%, indicating that nanoscale intergrowth of serpentine with brucite is unlikely. Moreover, no mixing of serpentine with brucite is detected in the Mg + Fe vs Si plot (Fig. S4).

As previously described by Kodolányi et al. (2012), amphibole is observed in some samples, and is considered to be the result of early hydration of mafic bodies at high temperature (ca. 400 °C). It is either associated with clinopyroxene as pargasite (S008, Iberia), or magnesiohornblende laths in some altered gabbro veins crosscutting the sample (S007, Newfoundland (Newfoundland), amphibole forms fragments of anthophyllite blades at the borders of a serpentine vein (Fig. 1B).

Carbonates have been observed in veins as late features in all four samples (e.g., Fig. 1A, F), and replacive carbonate in bastite in S012 (Iberia), S006 and S007 (Newfoundland, Fig. 1B and Fig. 1C, respectively). All carbonates were identified as calcite (Kodolányi et al., 2012). Described as 'seafloor weathering' by Kodolányi et al. (2012), carbonate precipitates in replacement of pseudomorphic serpentine within the bastite texture (S006 and S007, Newfoundland). In S012 (Iberia), carbonate crystallised in some mesh centres of the completely serpentinised part of the sample.

Some zones in the serpentine are Al-rich and could either result from mixing with chlorite, or represent an Al-rich serpentine (Oyanagi et al., 2018; Fig. S5). These Al-rich zones are observed in some mesh centres of S012 (Iberia) as highlighted in EPMA chemical maps (see Section 4.2, Fig. 2G–I), and were avoided for oxygen isotope and trace element measurements.

4.2. Major and minor element composition

The major element composition (Table S3 and Fig. 2) is used to validate the textural analysis presented above, which differentiates precursor minerals and different generations of serpentine within the same site. While this study focuses on serpentine texture, no analyses were performed on the mantle precursor minerals olivine and orthopyroxene, which are reported in Kodolányi et al. (2012). Major element maps were performed on samples S006 (Newfoundland), S008 and S012 (Iberia), but not S007. Fig. 2 displays element maps for Al_2O_3 (wt.%), SiO_2 (wt.%) and Cl (wt.%) for samples S006 (Newfoundland), and S008 and S012 (Iberia), the other maps are available in the supplementary

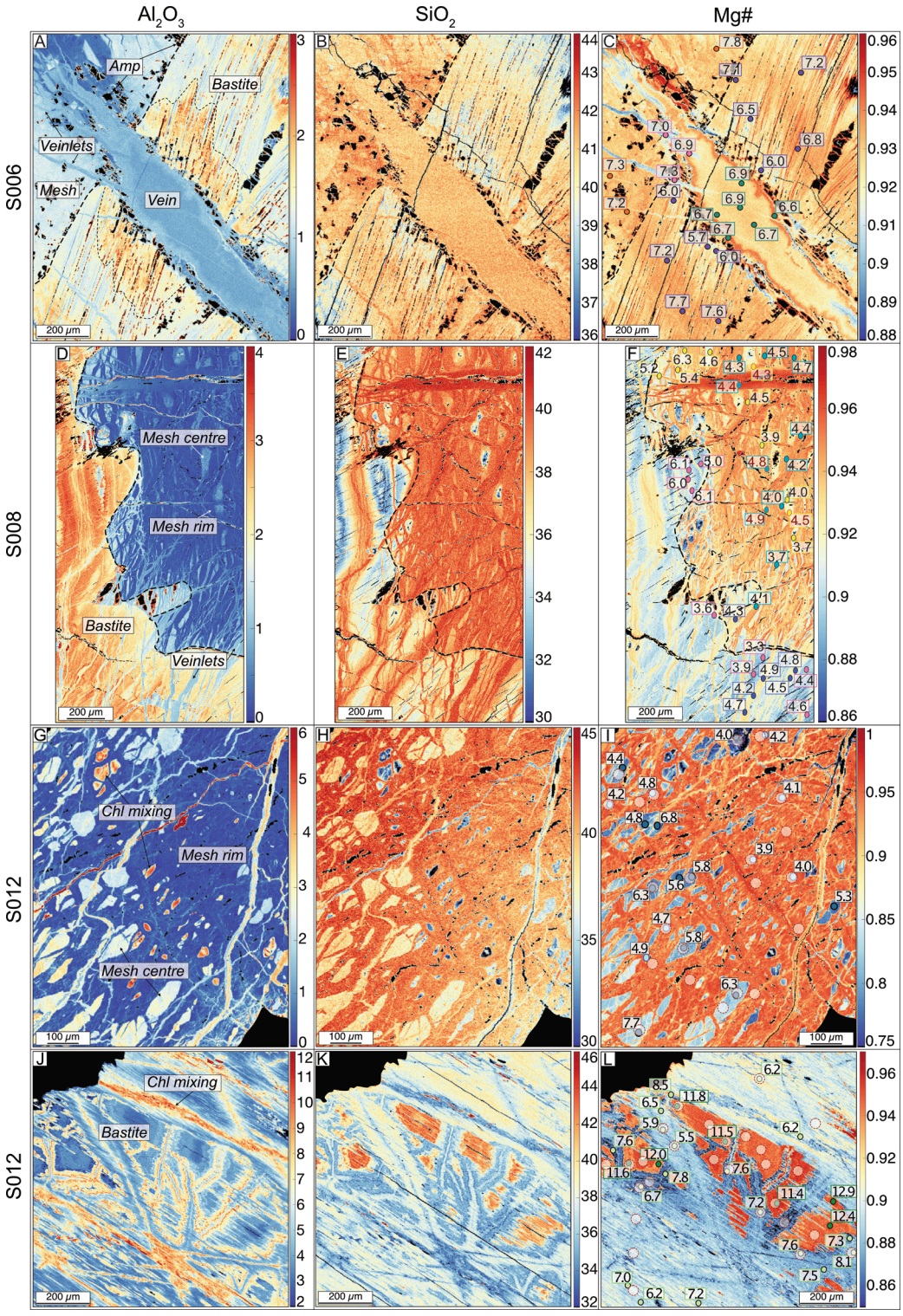

Fig. 2. Quantitative maps of serpentine for wt.% Al2O3 and SiO2, and Mg#. (A–C) Mesh, bastite and vein in sample S006 (Newfoundland). The black areas are amphiboles that were intentionally left out of the chemical maps. The zone of the bastite affected by the vein is highlighted with the black dotted line in map (A). (D–F) Bastite and mesh in sample S008 (Iberia). Note that the distinction between mesh rim and mesh centre was not visible in BSEimage (Fig. 1E), but is revealed by chemical maps. The black zones are pyroxene in the bastite domain, and magnetite in the mesh and bastite domains. Low Si domains in the mesh centre are due to porosity (E). (G–I) Mesh texture, both rim and centre in sample S012 (Iberia). The Al-rich zones can result from a mixing of serpentine with chlorite (G), or an Al-rich serpentine, consistent with low Si concentration in these zones. The black zones are magnetite (in the mesh network) and calcite (bottom right). (J–L) Zoned bastite in sample S012 (Iberia). The Al-rich zones are either due to the mixing of serpentine with chlorite, or an Al-rich serpentine, consistent with low Si content. The black zone on the top left corner is a calcite vein. The location of SIMS and LA-ICP-MS spots is shown on the Mg# maps, as well as the corresponding δ18O values in‰. Note that the Mg# maps consider all Fe as FeO.

material (Fig. S6).

4.2.1. Mesh texture

In the Newfoundland samples (S006 and S007), the serpentine in mesh texture shows SiO_2 contents varying between 38.81 and 42.24 wt % (all data are from spot EPMA analysis if not described otherwise; Table S3), which is within the typical silica range for serpentine minerals. The serpentine in mesh of S006 and S007 can contain up to 1.61 wt % Al_2O_3. In the Iberia samples S008 and S012, the serpentine in mesh rims have SiO_2 content from 37.23 to 41.54 wt%, whereas the serpentine in mesh centres show lower maximum silica content (37.5–39.88 wt%). The serpentine in mesh centres of S012 is associated to higher Al_2O_3 content than in the mesh rims (1.83–3.08 wt% versus <0.96 wt% in mesh rims). In sample S012 (Fig. 2G–I) the highest Al_2O_3 content of serpentine in both mesh rims and centres (up to 8.52 wt%) is associated with low SiO_2 = 35.07–37.41 wt%, revealing a significant chlorite microscale intergrowth with the serpentine, or an Al-rich serpentine (Fig. S5). These parts were avoided for further analysis. X-ray maps of

S008 (Fig. 2E–F) reveal zones with very low silica content in some mesh centres (<30 wt%), which have overall low totals. A mixing between serpentine and another phase is unlikely to produce these features, but it could be an effect of high porosity (Tutolo et al., 2016). These zones were avoided for oxygen isotope and trace element measurements. The trend of serpentine in mesh centres being Al-richer than mesh rims observed in S012 is also visible in S008 to a lesser extent (mesh centres serpentine data of S008 extracted from X-ray maps; Fig. 2D).

In both Newfoundland samples and S008, Mg# of serpentine is between 0.91 and 0.95. On the other hand, serpentinised olivine-websterite S012 displays significantly different serpentine Mg# between the mesh rim and the mesh centres, with Mg# = 0.92–0.96 and Mg# = 0.77–0.92, respectively (Fig. 2I). The serpentine in mesh centres of S012 contain up to 1.03 wt% NiO and 0.46 wt% MnO. The chemical maps of the serpentine in mesh centres of S012 also display low SiO_2 content correlated to lower Mg# (Fig. 2H–I). However, stoichiometric formula shows no Si deficit (Table S3), so the hypothesis of a mixing with another phase (e.g., brucite) is invalidated.

The chlorine content in S012 shows clear heterogeneity between the textures (Table S3). Chlorine is enriched in the serpentine in mesh centres (up to 0.23 wt%), but mostly lower than 0.1 wt% in the serpentine in mesh rims. Iberia sample S008 and both Newfoundland samples display similar variabilities of serpentine composition (Cl_{S008} = 0.04–0.2 wt%, Cl_{S006} = 0.07–0.27 wt%, Cl_{S007} = 0.12–0.31 wt%).

4.2.2. Bastite

Serpentine in bastite has SiO_2 = 37.55–41.78 wt% in the Newfoundland samples. A similar range is observed in the serpentine of S008 bastite from Iberia. In the elemental maps of bastite grain from S006 (Fig. 2A–C), the Si-poor zone in the serpentine in bastite surrounds the serpentine vein. In agreement with the precursor minerals (i.e., orthopyroxene), serpentine in bastite is Al-richer than the serpentine in mesh texture. In bastite, serpentine varies between Al_2O_3 = 0.71–3.37 wt% for S007 and Al_2O_3 = 1.62–3.17 wt% for S008. In S006, Al_2O_3 contents vary from the contact of the vein to the interior of the bastite (Al_2O_3 = 1.11–3.50 wt%) with Al-rich zones around the vein. Mg# of serpentine in S006 bastite is similar to the serpentine in mesh texture of the same sample, ranging from 0.89 to 0.93. S008 displays similar Cl content of serpentine in bastite as in serpentine in mesh domains (Cl = 0.06–0.20 wt%), whereas serpentine in bastite in S007 is richer in Cl up to 0.78 wt%, which is the highest concentration measured in our samples. Chlorine concentrations in serpentine from S006 are lowest around the vein, a zonation mirrored by silica and alumina concentrations (Fig. 2A, B).

Serpentinised olivine-websterite S012 shows larger variations in SiO_2, Al_2O_3, and Mg# (Fig. 2J–L). Three zones within a single pseudomorphic serpentine domain can be distinguished from rim to centre (highlighted in Fig. 1F): 'Bastite A', 'Bastite B', 'Bastite C' have increasing Mg# from 0.87–0.92 to 0.93–0.95 and 0.94–0.95, respectively.

4.2.3. Veins

Crosscutting veins in sample S006 (Fig. 2A–C) and S008 (Fig. 2D–F) are composed of lizardite with Mg# between 0.90 and 0.93. In S008, serpentine Si contents of the veinlets are higher than for the bastite but of the same range as for the mesh composition (SiO_2 = 38.0–40.5 wt%). Inversely, the serpentine alumina content of the veinlets is similar to that of the bastite and higher than that of the mesh, with Al_2O_3 > 0.7 wt %. The large vein serpentine in S006 has lower Al_2O_3 concentrations (<0.76 wt%) than the surrounding bastite. The element maps (Fig. 2A, C) show higher Al and Mg# at the vein border suggesting an interaction between the fluid in the vein and the surrounding serpentine.

4.3. Trace element compositions

In situ trace element compositions were determined for each texture in all the samples and normalised to primitive mantle (Fig. 3). The description here concentrates on the comparison between the different textural sites of the samples. When available, the composition of the primary minerals (mantle orthopyroxene and clinopyroxene, from Kodolányi et al. 2012) is shown to help detect trace element gain or loss during serpentinisation. Finally, limit of detection (LOD) concentrations are represented to illustrate the upper limit of concentration of the undetected elements.

Sample S012 (Iberia) shows trace element enrichment of serpentine in the mesh centres compared to the serpentine in mesh rims (Fig. 3D) and the different bastite serpentine zones (Fig. 3E, F), with most of the elements in the mesh centres above the bulk rock concentrations (Kodolányi et al., 2012). Similarly, in Iberia sample S008 (Fig. 3C), the serpentine in mesh centres display concentrations which are higher than the range in the heterogeneous serpentine in mesh rims. Moreover, in sample S008, the trace element concentrations measured in the bastite serpentine are distinctly higher than the bulk rock composition (except for Rb, Ba, Co, Zn, Ni; coloured highlights in Fig. 3C), while both the serpentine in mesh rim and centre have concentrations below those of the bulk rock. Comparing the trace element pattern of serpentine in bastite with the orthopyroxene pattern of sample S008 (Fig. 3C), most of the trace elements (La, Ce, Pr, Sr, Nd, Sm, Eu, Ti Gd and Li) are enriched in the serpentine compared to the primary mineral, with up to an order of magnitude increase in light rare earth elements (LREE), as well as Sr and Ti.

On the other hand, Zr and Ti contents in S012 are depleted in the serpentine mesh rims and centres compared to the bastite serpentine. This feature is seen in all the samples and can be explained by a precursor effect, with orthopyroxene being more enriched in Zr and Ti than mantle olivine (Rampone et al., 1991). The three bastite serpentine zones in sample S012 show generally similar concentrations, except for Rb which is higher in bastite serpentine C. The transition metal concentrations of serpentine in each bastite zone in S012 also vary and are discussed below.

4.3.1. Transition metals

The transition metals (V, Mn, Sc, Co, Zn, Ni, Cr) in serpentine may be indicative of the precursor mineral (e.g., Ni/Cr), but may also reflect element mobilization during serpentinisation. Manganese shows similar behaviour to that of Zn (Table S4), thus only Zn is discussed below and presented in Fig. 4. The concentration of transition metals of serpentine in mesh and bastite for all samples show opposite trends, when normalised to the primitive mantle (Fig. 3A–C). Fig. 4 shows the Ni/Cr ratio against selected transition metal concentrations for each texture of every sample, as well as the comparative mantle precursor composition (i.e., olivine and orthopyroxene, data from Sanfilippo et al., 2014; Kodolányi et al., 2012, respectively). The bastite serpentine shows a Ni/Cr ratio (Ni/Cr < 1) lower than that of the serpentine in mesh (Ni/Cr ≫ 1, Fig. 4), as the mantle orthopyroxene is enriched in Cr while the olivine is enriched in Ni.

Bastite serpentine in S006 (Newfoundland) shows relatively homogeneous transition metal concentrations (V 57–74 μg g^{-1}, Sc 19–25 μg g^{-1}, Co 33–52 μg g^{-1}, Zn 20–34 μg g^{-1}, Mn 600–900 μg g^{-1}, Table S4, Fig. 4 column 1) and a rather constant Ni/Cr ratio of 0.06–0.25. The mesh serpentine composition of S006 is more heterogeneous in Ni/Cr content and in the fluid immobile transition metals (i.e., V 4–73 μg g^{-1}, Sc 2–27 μg g^{-1}, Co 45–125 μg g^{-1}, Table S4, Fig. 4 column 1). The serpentine mesh composition ranges from that of the precursor olivine toward the bastite serpentine composition. The mesh and the bastite serpentines in S006 have the same concentration in the more fluid mobile transition metals Zn (Zn 20–29 μg g^{-1} and 22–37 μg g^{-1} respectively; Table S4). Whereas both mesh and bastite serpentine in S007 display up to an order of magnitude range in V and Sc concentrations, the other transition metals show a smaller range for serpentine in both textural sites (Fig. 4 column 2). While Ni content is moderately variable in the bastite serpentine (~760–1900 μg g^{-1}), Cr concentration

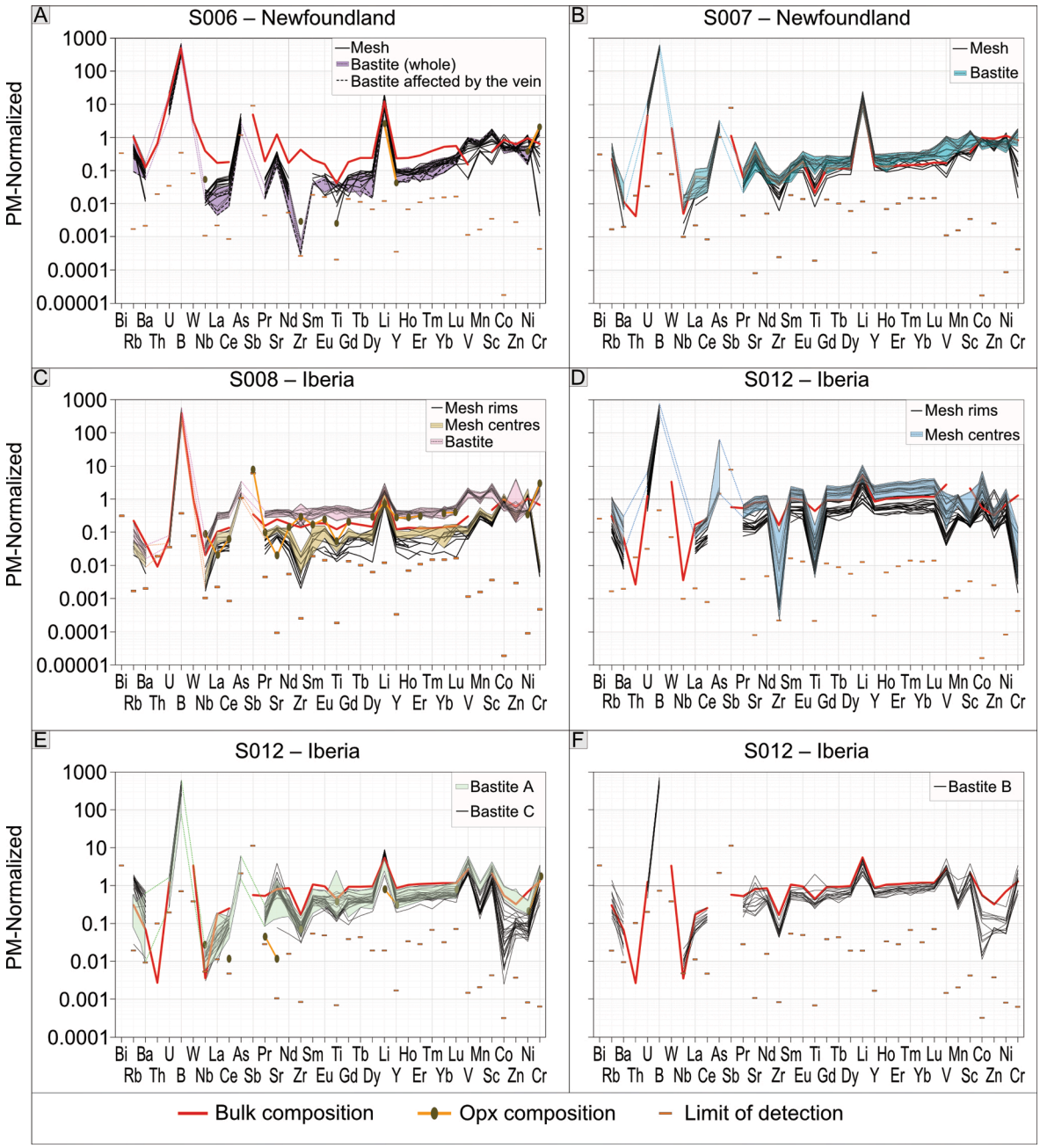

Fig. 3. Primitive mantle (PM) normalized (McDonough and Sun, 1995) trace element composition of serpentine in different textures from each sample. Trace element patterns for the respective bulk rock of samples are from Kodolányi et al. (2012). Trace element patterns for respective orthopyroxene composition from samples S006, S008 and S012 are from Kodolányi et al. (2012).

is particularly variable in the mesh serpentine (~40–1000 μg g^{-1}; Table S4, Fig. 4 column 2).

Unlike Newfoundland samples S006 and S007, serpentine in samples S008 and S012 from the Iberia passive margin is closer in composition to the primary precursor mineral, especially in Ni/Cr ratio (Table S4, Fig. 4 column 3 and 4). The transition metal contents of S008 bastite serpentine are close to the orthopyroxene precursor, except for Zn, which shows depletion. Bastite serpentine in S012 is more variable in Ni/Cr and in Sc, Co and Zn (up to 2 orders of magnitude). Vanadium contents show the least variation. The extreme variability in Co content in S012 bastite serpentine domains follows the bastite formation sequence, with serpentine in bastite A being richer in Co, bastite B having intermediate values and bastite C having the lowest concentration ($Co_{bastite\ A}$ 45–100 μg g^{-1} to $Co_{bastite\ C}$ 0.25–22 μg g^{-1}.). This trend is also visible for Zn (and Mn, Table S4). Serpentine in mesh rims and the mesh centres of S012 have distinct composition, mesh centres serpentine are richer in Co and Zn than mesh rims serpentine (Co 24–200 μg g^{-1} and Zn 4–14 μg g^{-1} in the mesh rims, Co 110–670 μg g^{-1} and Zn 9–28 μg g^{-1} in the mesh centres, Fig. 4 column 4). Vanadium and Sc concentrations in mesh rims and mesh centres serpentine are distinct, although partly overlapping, in sample S012 (V 3–100 μg g^{-1} and Sc 2.2–4.5 μg g^{-1} in the mesh rim, V 10–150 μg g^{-1} and Sc 3–25 μg g^{-1} in the mesh centres, Fig. 4 column 4). Scandium concentrations are comparable between the two Iberia samples, but V content is less variable in sample S008 (V 5–12 μg g^{-1} for serpentine in both mesh rim and centre).

Overall, we observe a redistribution of V, Sc, Co, Ni and Cr between serpentine in mesh and bastite in Newfoundland samples S006 and S007. In Iberia samples S008 and S012, there is a redistribution of V

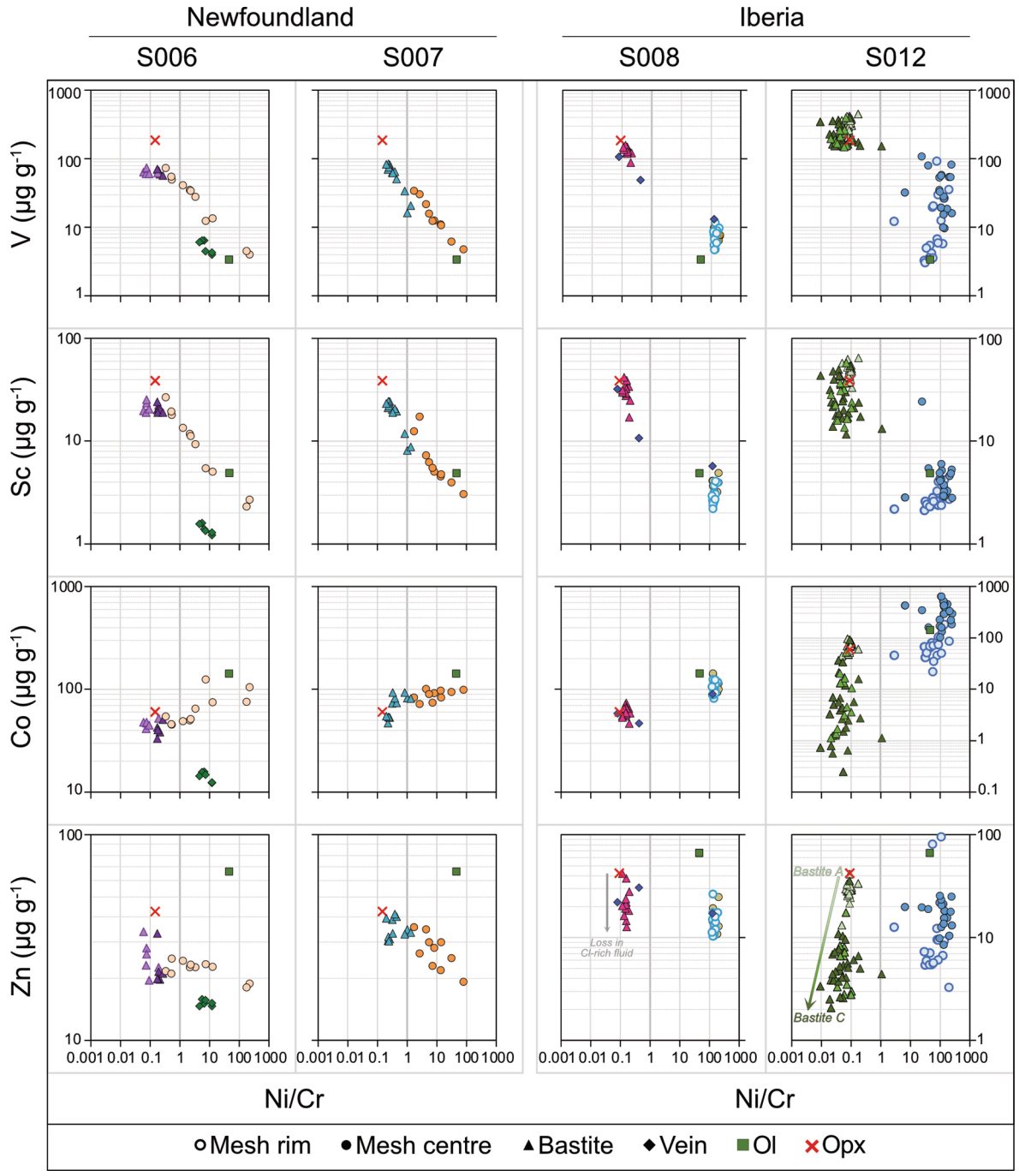

Fig. 4. Transition metals (V, Sc, Co and Zn) versus Ni/Cr ratio in serpentine from the different samples. Note that for S006 and S007, the circles represent the mesh without distinction between rim and centres. The mantle orthopyroxene compositions are from Kodolányi et al. (2012) for the respective samples S006, S008 and S012. The mantle orthopyroxene composition of sample S006 was used for sample S007. Representative mantle olivine compositions for all the samples are from Sanfilippo et al. (2014). Symbols for each textural domain are reported in the legend and apply to all samples; colours are distinct for every sample and applied to all figures.

between the mesh rim, mesh centres and bastite serpentine, and a general loss of Co, Zn, Mn (Fig. 4).

4.3.2. *Chlorine and Boron*

We observe that in both Newfoundland samples, the serpentine Cl distribution in the textural sites (mesh and bastite) is similar, but more enriched in S007 than in S006 (Cl_{S006} 1200–2700 µg g^{-1} and Cl_{S007} 2000–7400 µg g^{-1}, Fig. 5A, B) at roughly equal B (B_{S006} 90–200 µg g^{-1} and B_{S007} 100–190 µg g^{-1}, Fig. 5A, B). This results in a Cl/B of about 10 for sample S006 (Fig. 5A), while in sample S007 (Fig. 5B), serpentine in mesh and bastite have a Cl/B of about 15 and higher. In Newfoundland samples S006 and S007, B is positively correlated with U, suggesting that U got enriched during hydration (Table S4 and Fig. S7). Iberia samples S008 and S012 show distinct concentrations of serpentine between the mesh and the bastite. In sample S008, B and Cl are higher in the bastite serpentine than the mesh serpentine, with a variable Cl/B for the bastite (Fig. 5C), whereas the mesh serpentine has a constant Cl/B of 20. In sample S012, serpentine in the different bastite domains is remarkably variable in B, but mostly poorer in Cl than the mesh serpentine, with the exception of serpentine in bastite C that is partly Cl-

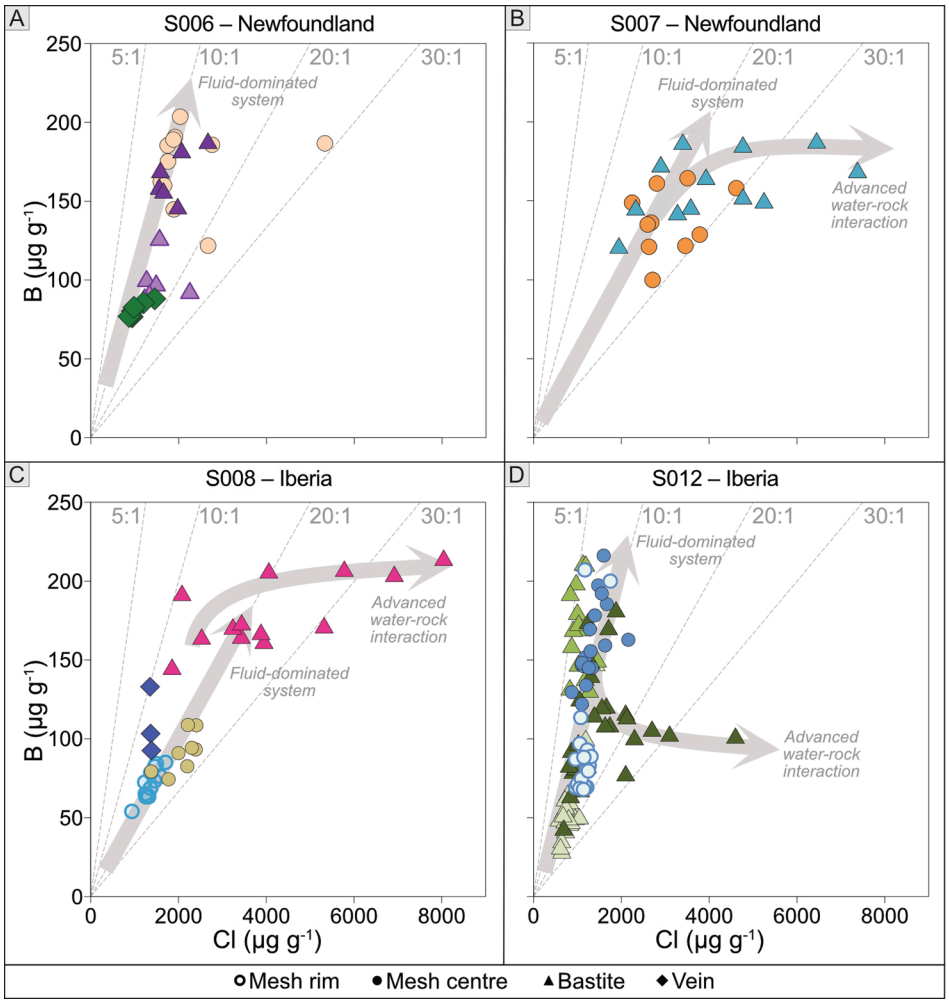

Fig. 5. LA–ICP–MS Cl versus B contents in serpentine of the different samples. The grey dashed lines represent a constant Cl/B ratio of 5, 10, 20 and 30, respectively. The grey arrows illustrate the expected trend of the evolution of Cl and B composition in serpentine for progressive serpentinisation with advanced water–rock interaction (Cl/B increases) or for serpentinisation in a fluid-dominated system (constant Cl/B). The symbols for each textural domain are reported in the legend and the colours are different for every sample.

rich (Fig. 5D). In this sample the variation in Cl/B is large and the overall Cl and B contents are lower than in sample S008.

4.3.3. Veins

Two samples display serpentine vein textures (S006 from Newfoundland, S008 from Iberia). The serpentine vein in sample S006 has the lowest Cl and B contents in the sample (Fig. 5A), as well as low transition metal concentrations (Fig. 4 column 1). The bastite serpentine close to the vein shows lower trace element concentrations than the rest of the bastite serpentine (e.g., REE, FME) (Fig. 3A, dashed line). There is a gradient in the serpentine trace element concentrations, mirrored by major elements Al and Mg#, from the depleted vein to the initial bastite. In sample S008, the serpentine veinlets have a composition similar to the initial serpentine texture they cut (e.g., in the transition metals, Fig. 4 column 3).

4.4. Oxygen isotope compositions of serpentine textures

The oxygen isotope compositions of serpentine were measured *in situ* to ensure textural control (i.e., mesh rim, mesh centre, bastite and vein). The $\delta^{18}O$ results are shown in Fig. 6, plotted by sample and serpentine texture, and the SIMS spot locations with measured $\delta^{18}O$ values are provided in the elemental maps in Fig. 2C, F, I, L. The detailed dataset of $\delta^{18}O$ is given in Table S5.

Serpentine in Newfoundland samples S006 and S007 display variability in $\delta^{18}O$ of <3‰ between different textural domains, which largely overlap in a given sample. Generally, serpentine $\delta^{18}O$ values are at or slightly above the mantle range ($\delta^{18}O = 5.5 \pm 0.5$‰, Mattey et al. 1994). For sample S006, the isotopic variability of bastite serpentine is correlated with the distance from the serpentine vein. Serpentine in the bastite near the vein is Al-rich, Si- and Cl-poor, and shows a lighter isotopic composition ($\delta^{18}O = 5.6$–6.5‰, light purple triangle in Fig. 6), whereas lizardite in bastite further from the vein has $\delta^{18}O = 6.4$–7.7‰ (dark purple triangle in Fig. 6). Two vein types were analysed in S006, both having the same narrow isotopic composition of $\delta^{18}O = 6.8$–7.4‰.

Serpentine in sample S008 from Iberia displays a similar range in $\delta^{18}O$ as the Newfoundland samples (~3‰), however, the $\delta^{18}O$ values extend to below the mantle compositional range with serpentine $\delta^{18}O_{\text{mesh rims}} = 3.7$–$4.7$‰, $\delta^{18}O_{\text{mesh centres}} = 3.7$–$6.3$‰ and $\delta^{18}O_{\text{bastite}} = 3.3$–$6.1$‰. The serpentine veinlets in S008 have a homogeneous composition of 4.2–4.9‰, overlapping with the ranges of serpentine in mesh and bastite textural domains. In contrast, serpentine in sample S012 from Iberia shows a pronounced variation in $\delta^{18}O$ between textural positions ($3.9‰ < \delta^{18}O < 13.5‰$), from below the mantle range for serpentine in mesh rim to distinctly above the mantle composition for all bastite serpentine types. The serpentine in mesh rims has an oxygen isotopic composition of 3.9–4.9‰, while the mesh centres serpentine have $\delta^{18}O$ values ranging from 4.0 to 8.6‰. Serpentine in the bastite with multiple zones are also characterised by distinct isotopic compositions, which are not correlated to Mg# and are systematically above the mantle range (Fig. 6): $\delta^{18}O_{\text{Bastite A}} = 5.5$–$8.5$‰, $\delta^{18}O_{\text{Bastite B}} = 11.4$–$13.5$‰, $\delta^{18}O_{\text{Bastite C}} = 8.5$–$12.9$‰.

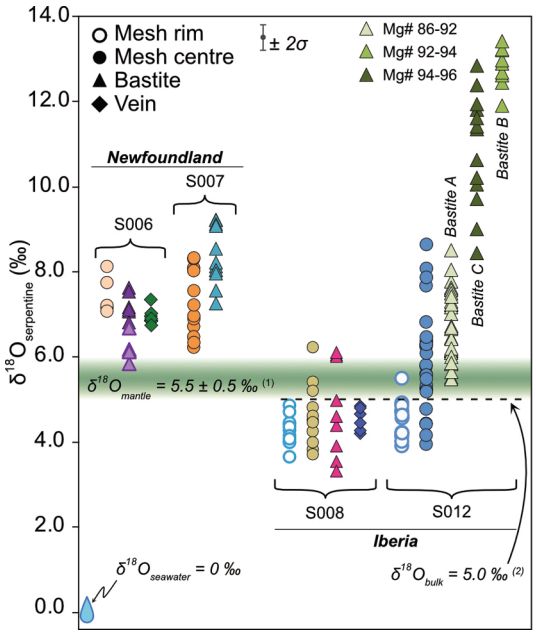

Fig. 6. *In situ* oxygen isotope composition of serpentine sorted by textures and samples. The green band represents the δ18O composition of the mantle ((1) Mattey et al., 1994). Oxygen isotope bulk composition of serpentinites at depth of our sample in ODP Site 1070 is represented by the dashed line ((2) Skelton and Valley, 2000). The maximum internal error of single measurements is shown at the top of the diagram (σ; 0.3‰, 2 s). The symbols for each textural domain are reported in the legend and the colours are different for every sample.

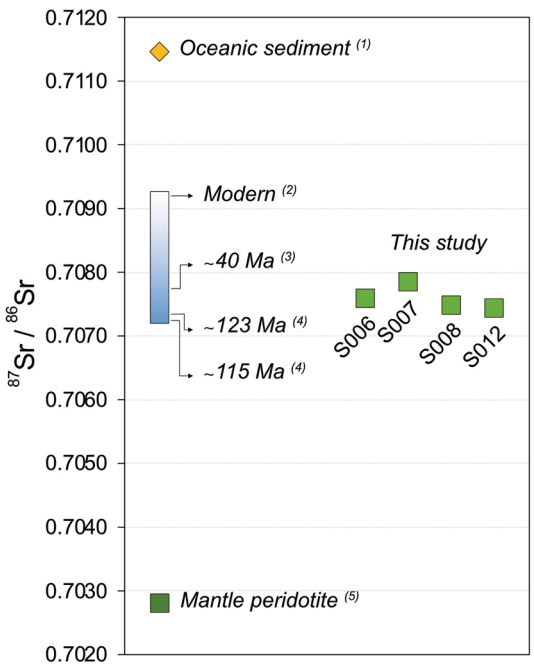

Fig. 7. Strontium isotope composition on bulk rock samples (data from Table S2) compared to that of mantle peridotite 87Sr/86Sr = 0.7028 (5) McCulloch et al. (1981), oceanic sediment and seawater of different ages. Literature data are from (1) Ben et al. (1989), 87Sr/86Sr = 0.711465; (2) Elderfield (1986), 87Sr/86Sr = 0.7092; (3) Hess et al. (1986), 87Sr/86Sr = 0.707747 ±; 34; (4) Jones et al. (1994), 87Sr/86Sr = 0.707378 ±; 28 at ~123 Ma, 87Sr/86Sr = 0.707252 ±; 10 at ~115 Ma. The 87Sr/86Sr ratio of the seawater fluctuates between 123 and 40 Ma, and increases linearly from 40 Ma onwards. The error bars are within the symbols size.

4.5. Strontium isotope composition of bulk rock

Strontium isotope data for the four serpentinite samples have a narrow range from $^{87}Sr/^{86}Sr_{S012}$ = 0.707440 ± 2 to $^{87}Sr/^{86}Sr_{S007}$ = 0.707850 ± 4 (Table S2, Fig. 7). The two Newfoundland samples have slightly more radiogenic values ($^{87}Sr/^{86}Sr_{S006}$ = 0.707594 ± 3, $^{87}Sr/^{86}Sr_{S007}$ = 0.707850 ± 4) while samples from Iberia have lower values of 0.707479 ± 4 and 0.707440 ± 2. The timing of the asthenospheric upwelling, i.e., prior to or coeval with the subcontinental mantle exhumation, has been dated to ~124 Ma for Site 1070 (Iberia margin), and at ~115 Ma for Site 1277 (Newfoundland margin; Eddy et al., 2017). At the time of the onset of the embryonic slow-spreading oceanic ridge, the Sr isotope ratio of seawater reached its minimum at $^{87}Sr/^{86}Sr$ = 0.70725 (e.g., Elderfield, 1986). Therefore, the samples have Sr isotope ratios only marginally higher than that of seawater contemporaneous with serpentinisation.

5. Discussion

The combined trace element and oxygen isotope data document different serpentinisation processes for Newfoundland and Iberia passive margin localities. Transition metals are particularly well suited to distinguish between simultaneous and sequential serpentinisation of the mantle olivine and orthopyroxene sites. The trace element composition of serpentine from this study is compared with that of mantle olivine and orthopyroxene. While the trace element signature of orthopyroxene for these samples was reported by Kodolányi et al. (2012), olivine is absent in this sample set. Because of a lack of *in situ* trace element composition of mantle olivine in harzburgite from oceanic settings, we use mantle olivine geochemistry data from obducted plagioclase-harzburgites (from Serra Debbione and the Internal Ligurian ophiolites, Sanfilippo et al., 2014). Unfortunately, because of its fine grain size (<0.1–5 μm), there are no geochemical data for magnetite formed during oceanic serpentinisation, so the effect of magnetite cannot be discussed. The fluid mobile element compositions of serpentine are used to track the evolution of the fluids and to distinguish a fluid-dominated system from an evolved fluid after advanced water–rock interaction. The oxygen isotope composition of the serpentine can be controlled by several parameters with temperature exerting a primary control (see Section 5.3). Coupled with the trace element data, they help to characterise the multistage hydration history of oceanic serpentinisation.

5.1. Transition metal systematics: simultaneous versus sequential serpentinisation

The concentration of elements considered to be relatively immobile during alteration can be relevant for (i) confirming the correct identification of mesh versus bastite sites, (ii) identifying different serpentinisation conditions in each sample, and (iii) constraining the relative timing of hydration of the olivine and pyroxene sites. In the investigated samples, two distinct transition metal behaviours between mesh and bastite are observed. In the Iberian passive margin samples, mesh and bastite retain compositions indicative of precursor olivine and orthopyroxene, documenting limited transition metal mobility during serpentinisation. In contrast, Newfoundland samples show a strong redistribution of transition metals between textural sites, which results in a range of transition metal concentrations across all textural serpentine domains. This indicates that the distance of equilibration exceeded that of the precursor mineral grain size.

A particularly good discriminator between olivine and orthopyroxene is Ni/Cr. Relict olivine is not present in the investigated samples, but mantle olivine generally has a high Ni/Cr ratio (>30 for olivine in obducted ophiolites, Sanfilippo et al., 2014), and thus serpentine crystallising in the mesh texture is expected to have a high Ni/Cr. On the other hand, pseudomorphic replacement of orthopyroxene in the bastite texture is expected to retain a low Ni/Cr of about 0.14 for S006 and 0.09

for S008 and S012, respectively (orthopyroxene trace element composition from Kodolányi et al., 2012). The resolving power of Ni/Cr between olivine and orthopyroxene precursors is of several orders of magnitude, up to 100 (x-axis in Fig. 4), which is sufficient to differentiate serpentine crystallising after olivine or orthopyroxene.

Transition metal systematics are straightforward for the Iberia samples (Fig. 4). Ni/Cr ratios for serpentine in mesh and bastite are distinct and correspond to those of the olivine and orthopyroxene precursors. In sample S008, Sc, Co, and V show the same distinct clustering around precursor olivine and orthopyroxene, except for V in mesh serpentine, which is enriched by up to an order of magnitude relative to magmatic olivine, ranging between 5 and 10 μg g^{-1}. We suggest that this V enrichment may signal magmatic sulphide decomposition during serpentinisation of olivine. The deviations in Cr, Sc and Co contents in serpentine from the precursor olivine and orthopyroxene could be induced by the crystallisation of co-products such as magnetite or sulphides during serpentinisation. Micrometric magnetite grains are observed in all samples, and pentlandite, pyrrhotite and pyrite have been reported in the literature in Iberian drill sites (e.g., Alt and Shanks, 1998). Moreover, possible effect of magmatic sulphide relics and newly formed sulphides on trace element systematics were discussed in Kodolányi et al. (2012). We interpret the different trace element patterns of mesh and bastite in sample S008 as evidence for insignificant serpentine equilibration between mesh and bastite textural sites, suggesting that serpentinisation of olivine and orthopyroxene occurred sequentially, according to reactions (1) and (2) above, rather than simultaneously.

Serpentine in sample S012 from Iberia displays a larger range of Ni/Cr, V and Sc concentrations when compared to sample S008, but the mesh and bastite domains still maintain distinct compositional arrays (Fig. 4). In the mesh serpentine, Co and Sc concentrations cluster around the precursor olivine, with a notable difference between mesh centre and mesh rim. We interpret this to indicate a short-range migration of Co and Sc from mesh rims towards mesh centres during progressive serpentinisation of olivine. For bastite crystallisation stages, bastite A resembles the precursor orthopyroxene most closely, while bastite B and C deviate towards lower concentrations of Sc and notably Co. Alt and Shanks (1998) reported rare siegenite ($CoNi_2S_4$) and Co-pentlandite ($(NiFeCo)_9S_8$) in the Iberia passive margin serpentinised peridotite from Sites 637 and Site 897, which could cause the depletion of Co in bastite compared to precursor orthopyroxene in sample S012. Overall, the transition metal systematics suggest that sample S012 records a more complex serpentinisation history than sample S008, but still with likely sequential olivine and orthopyroxene serpentinisation, as indicated by the distinct transition metal concentration in mesh and bastite.

In the Newfoundland samples S006 and S007, the data for mesh and bastite serpentine document different systematics. While bastite in sample S006 largely retains a uniform Ni/Cr of the precursor orthopyroxene, bastite in sample S007 ranges towards the mesh composition in Ni/Cr, V, Sc and Co. Bastite in both samples is moderately depleted in V and Co compared to the orthopyroxene precursor, each by a factor of three (Fig. 4). In mesh serpentine, Ni/Cr and V, Co, and Sc contents trend between those of the precursor olivine and orthopyroxene. The compositional trends between mesh and bastite domains are attributed to fluid-induced mobilisation of Ni, Cr, V, Co, and Sc over distances exceeding the crystal sizes of the peridotite precursor, estimated to be of the order of 1 cm. This indicates that serpentinisation of the two sites occurred simultaneously according to reaction (3) above.

Zinc and Mn (Fig. 4 and Table S4) display different systematics than other transition metals because both elements are fluid-mobile in presence of Cl-bearing fluids (Xing et al., 2022). Serpentine in both mesh and bastite is systematically depleted in Zn with respect to mantle olivine and orthopyroxene. This behaviour could indicate that Zn and Mn are lost to the fluid during serpentinisation (more evident in mesh serpentine) or that a Zn- or Mn-bearing phase formed during serpentinisation sequestered these elements such as sphalerite (if there is significant H_2S in the fluid to form sphalerite; Seyfried and Dibble, 1980). No such phases have been reported in the rocks of the Iberia or Newfoundland drill sites. Hence, concurrent sulphide crystallisation during serpentinisation cannot account for Zn depletion. Removal by the fluid phase is thus the most likely process to account for Zn (and Mn) depletion in serpentine relative to precursor olivine and orthopyroxene.

5.2. Evolution of the fluid composition with progressive serpentinisation

Oceanic serpentinisation has long been known to produce specific FME enrichments in serpentine minerals, in particular B (Scambelluri et al., 2004; Vils et al., 2008; Kodolányi et al., 2012), As and Sb (Kodolányi et al., 2012), U but not Th (Kodolányi et al., 2012), and the halogens Cl and Br (Scambelluri et al., 2004; Vils et al., 2008; Kodolányi et al., 2012; Kendrick et al., 2013). In a PM-normalised trace element distribution diagram (Fig. 3), the passive margin serpentine data display variably pronounced enrichments in B, U, As, Li, ±Rb, and ±Sr, demonstrating the presence of a characteristic FME imprint of oceanic hydration.

The required minimum water–rock ratio during serpentinisation is controlled by the stochiometric incorporation of water H_2O into serpentine and other hydrous minerals (addition of 2 H_2O molecules to the initial olivine structure of 7 atoms, 2/7 = 0.285, Wenner and Taylor, 1973). The bulk Sr isotopic composition of the serpentinised peridotites has implications for the water–rock ratio. The samples used in this study fall within the range of the Cretaceous seawater composition (~115 Ma, Fig. 7) to the modern seawater composition, far from the mantle peridotite value and without evidence of contamination by oceanic sediments. Thus, the Sr isotopic composition indicates that hydration of the peridotite in these samples generally occurred at high water–rock ratios, in agreement with the observed high degree of serpentinisation. Potential post-serpentinisation processes (e.g., subseafloor weathering, carbonate precipitation) would shift the Sr isotope data toward the ambient seawater composition, resulting in an overestimation of the water–rock ratio. In the case of carbonate precipitation formed from sediment-equilibrated fluids, the Sr isotope signatures may become more radiogenic than ambient seawater. The latter is not what is observed in this study, and the potential influence of oceanic sediments is discarded. Despite of the ~85 m (Site 1277, Newfoundland margin) to ~660 m (Site 1070, Iberia margin) pile of sediment on top of the serpentinised mantle (Fig. S1), the sediment cover did not contaminate the Sr isotope ratio of the samples. Moreover, the study of the brucite-calcite veins in serpentinites from Leg 149 Site 897 (Iberian margin) suggests that serpentinisation fluid was mixed with seawater below the seafloor (Klein et al., 2015). These last two points suggest that sedimentation probably occurred after serpentinisation and that the incorporation of fluid mobile elements in the serpentine was seawater-driven. Additional constraints on the water evolution, especially salinity, come from the relative concentration of water-sourced elements in serpentine, such as Cl and B.

There is a large variability in Cl and B contents within and between samples (Fig. 5), with serpentine in certain domains having either constant or variable Cl/B ratio. Since both Cl and B are sourced from seawater (initial composition of Cl ~19000 μg g^{-1} and B ~4 μg g^{-1}, Uppström, 1974), their distribution in the serpentine may track different hydration events and possibly the salinity of the fluid (Fig. 8). If B and Cl incorporation into serpentine is determined solely by serpentine-fluid distribution coefficients, a constant Cl/B ratio in serpentine within a given textural domain would be expected. Experiments have been performed on the fluid–solid partitioning of B (Hansen et al., 2017), but to our knowledge there are no experimental or empirical data for fluid-serpentine Cl partitioning, so we use our data to obtain first-order estimates. Using the concentrations of Cl and B in seawater (Uppström, 1974) and in serpentine vein of sample S006 (~900 and 80 μg g^{-1}, respectively, Table S4), we obtain $KD_{serpentine/seawater}$ for Cl = ~0.05 and for B = ~15. Our value agrees well with the partition coefficients

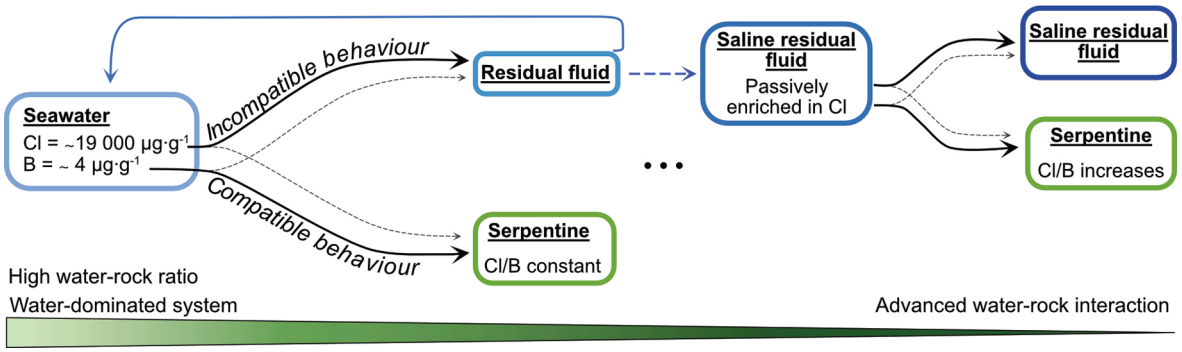

Fig. 8. Conceptual illustration of the fractionation of Cl and B from the seawater into serpentine and residual fluid, in a fluid-dominated system and after an advanced water–rock interaction. Chlorine is incompatible and preferentially stays in the fluid while B is incorporated into serpentine during water–rock interaction. In a fluid-dominated system, the fractionation of Cl and B between serpentine and the residual fluid does not vary, and Cl/B in serpentine is constant. In the scenario of an advanced water–rock interaction, the residual fluid becomes saline after a passive Cl enrichment. The Cl-rich serpentine reflects a fluid richer in Cl than seawater, and this induces an increase of Cl/B in serpentine.

measured by Hansen et al. (2017); $KD(B)_{solid/fluid}$ 24 and 13 at 100 °C and 200 °C, respectively. Our data thus show that Cl is incompatible in serpentine and preferentially remains in the residual fluid, whereas B is compatible in serpentine. Our measured Cl and B concentrations in serpentine are consistent with data previously reported for oceanic serpentine from other locations (Agrinier et al., 1988, 1996; Früh-Green et al., 1996; Mevel and Stamoudi, 1996; Barnes and Sharp, 2006; Beard et al., 2009; Deschamps et al., 2011; Kodolányi and Pettke, 2011; Kodolányi et al., 2012; Rouméjon et al., 2018, 2019, 2015); hence, we consider our estimates of B and Cl fluid-serpentine distribution coefficients to be robust.

Mesh is generally characterised by a uniform Cl/B for a given sample, suggesting that the mesh may preferentially form in a fluid-dominated system. The difference in Cl/B of the mesh from different samples could be due to two end-member factors, or a combination of them: (i) the dependence of $KD_{serpentine/seawater}$ for B and/or Cl on temperature, or (ii) variable Cl/B of the hydrating fluid. These two factors cannot be disentangled with the present data.

An evolving Cl/B ratio within a single textural domain is expected in the case of limited fluid supply interacting with the rock. The most extreme case would be a scenario where a given mass of peridotite reacts with a given mass of seawater to progressively produce serpentine in a "closed system". This scenario leads to a progressive increase in Cl/B ratios during serpentinisation, as the fluid becomes increasingly enriched in Cl compared to B which is compatible in serpentine. This results in a saline residual fluid depleted in B. Since the serpentine composition in terms of Cl and B is controlled by the fluid, a progressively increasing Cl/B ratio in the serpentine with decreasing fluid/rock ratio is to be expected. This makes Cl/B an indirect proxy for water–rock ratio. Bastite C of sample S012 is an example of such a near-closed-system scenario, not only because of its zoned texture (Fig. 1F), but also because of the trend of increasing Cl with decreasing B contents (Fig. 5D), consistent with the model evolution line of the seawater composition in a closed system. The extreme Cl enrichment observed in some samples (up to 8000 µg g^{-1}, e.g., Fig. 5B, C) could additionally reflect the crystallisation of submicrometric phases enriched in Cl (e.g., iowaite, Kodolányi et al., 2012; salt crystals, Sharp and Barnes, 2004) whose subtle presence would contaminate the serpentine analysis. The trends of increasing Cl/B for bastite in S007 and S008 indicate that such a hydration process may be common for the serpentine crystallisation in the bastite texture. Consequently, if the Cl/B ratio does not increase in a serpentine textural domain, this provides evidence for "open system" serpentinisation.

The use of *in situ* B and Cl compositions in serpentine gives a good insight into the open versus closed system hydration systematics, and the subsequent evolution of the fluid composition. While a constant Cl/B ratio indicates an open system with constant Cl and B concentrations in the hydration fluid and a constant fractionation factor between the fluid and the serpentine, an increasing Cl/B with progressive serpentinisation suggests an increase in fluid salinity after significant water–rock interaction in a near-closed system. The trace element systematics do not constrain serpentine formation temperatures because it is unknown whether $KD_{serpentine/seawater}$ for a given trace element varies with temperature, and thus an independent geochemical tool is needed to investigate the temperature of serpentinisation.

5.3. *Oxygen isotope systematics: effect of temperature and fluid composition*

The factors controlling the $\delta^{18}O$ composition of minerals are: (i) temperature, (ii) water–rock ratio, (iii) oxygen isotopic composition of the fluid, and (iv) the oxygen isotopic composition of the rock undergoing alteration (Taylor, 1977). In the investigated samples, the oxygen isotopic composition of the parent rock can confidently be assumed to correspond to mantle peridotite with $\delta^{18}O = 5.5 \pm 0.5‰$ (Mattey et al., 1994). The range of isotopic compositions for the serpentinising fluid is generally considered to be between that of seawater (0‰) and that of the heaviest seawater-derived fluid ever sampled in a natural environment (2.4‰; Snake Pit vent field, Mid-Atlantic Ridge at Kane site 23°22′N, Campbell et al., 1988). This range is a good assumption for the initial fluid composition, but higher $\delta^{18}O$ fluids cannot be excluded and could be expected in regimes with low water–rock ratios. The water–rock ratio is a challenging parameter to determine, but can be indirectly monitored with Cl/B (see Section 5.2).

The O isotopic composition of serpentine can be used to determine the temperature of serpentinisation if the O isotopic compositions of rock and water at the time of hydration are known. The $\Delta_{serpentine\text{-}fluid}$ geothermometer was first developed by Wenner and Taylor (1971), and the fractionation factors were revised by Früh-Green et al. (1996) and Saccocia et al. (2009). More recently, Vho et al. (2019) revised the fractionation factors within an internally consistent database, which is used in this study together with the dataset from Zheng (1993). In general, the passive margin settings are known to have undergone cold serpentinisation, as inferred by $\Delta^{18}O_{serpentine\text{-}magnetite}$ (<200 °C, e.g., Agrinier et al., 1996), and by $\Delta^{18}O_{serpentine\text{-}fluid}$ (<50–200 °C, e.g., Skelton and Valley, 2000). Skelton and Valley (2000) measured serpentine mesh separates from serpentinites and serpentinite clasts for Iberian Sites 1068 and 1070, and calculated temperatures (50 to >175 °C) assuming a seawater composition ($\delta^{18}O$ = 0‰), i.e., high water–rock ratios. Moreover, it has been proposed that magnetite-poor serpentinisation is diagnostic of low temperature alteration (<200 °C, Klein et al., 2014). Our observations of magnetite-poor samples, in line

with previous observations (e.g., Kodolányi et al., 2012), and together with the low magnetic susceptibility data of the core samples (Whitmarsh et al., 1998; Tucholke et al., 2004) suggest that the samples from Iberia and Newfoundland were serpentinised at temperatures <200 °C. Variability in the *in situ* O isotopes suggests temperature variations during the serpentinisation process.

Coupling of $\delta^{18}O$ and Cl/B ratio in serpentine, enabled by spatially resolved *in situ* correlation, is used to unravel the influence of temperature and fluid composition, resulting in different scenarios (Fig. 9A):

I. Constant Cl/B and variable $\delta^{18}O_{serpentine}$ implies a fluid-dominated hydration environment with constant fluid composition; hence, temperature is the parameter driving the variability in $\delta^{18}O_{serpentine}$.
II. Constant $\delta^{18}O_{serpentine}$ combined with an increasing Cl/B ratio in the serpentine suggests that the O isotope signature of the serpentinising fluid remained constant despite an increase in fluid salinity;
III. An increase in both $\delta^{18}O_{serpentine}$ and Cl/B may result from a decrease in hydration temperature and/or fluid compositional evolution; however, distinguishing between these cases is not straightforward.

Using this concept and considering the transition metal information on chemical exchanges between sites, the serpentinisation process at each site can be constrained.

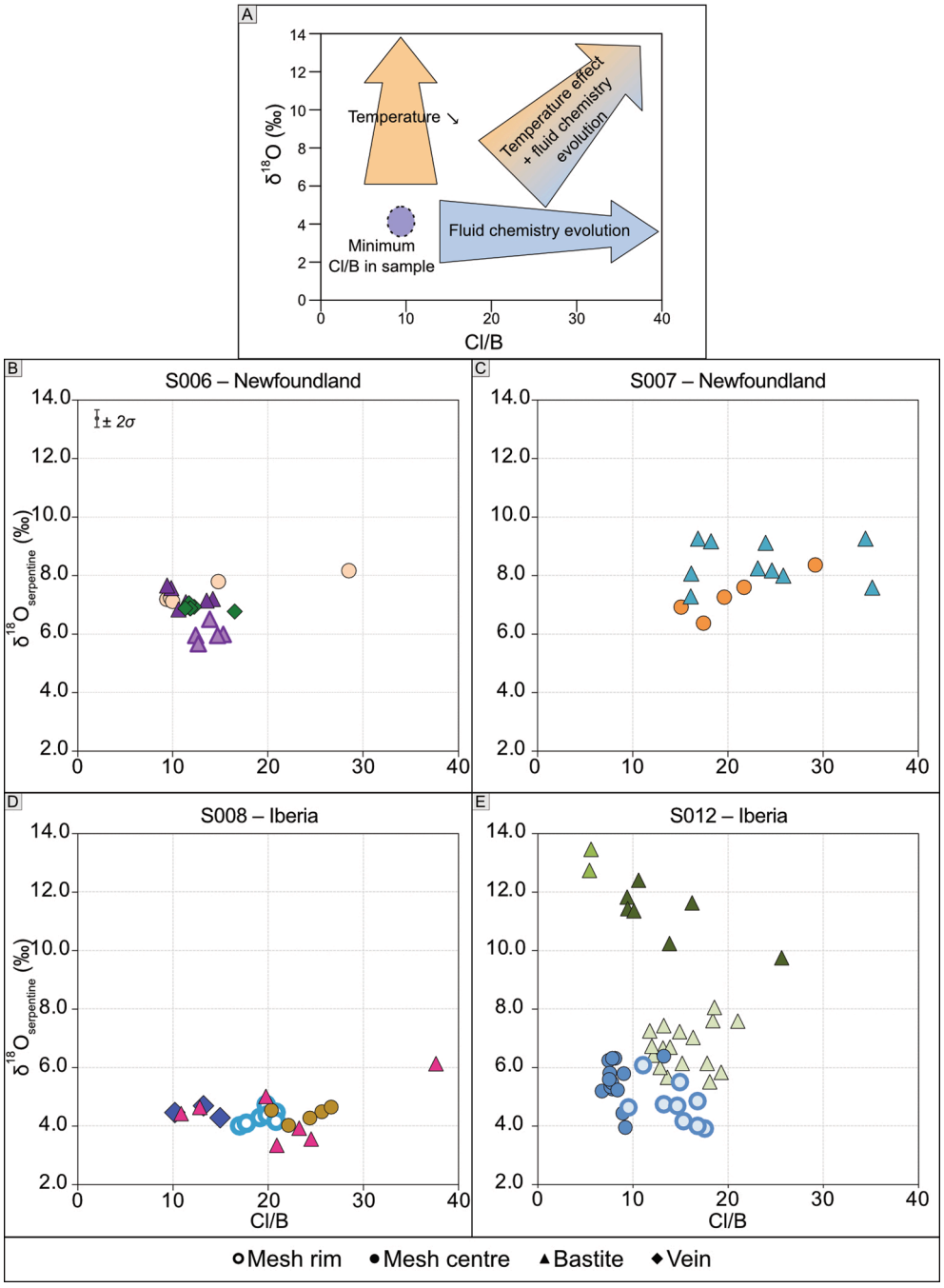

Fig. 9. (A) Sketch summarizing the effect of fluid chemistry evolution (horizontal arrow) and temperature on the oxygen isotope composition (vertical arrow) of the serpentine phases. (B–E) Plots of Cl/B ratio versus $\delta^{18}O$ for the investigated samples. The error bar shown on panel (B) represents the maximum internal error of single oxygen isotope measurements: σ; 0.3‰ (2 *s*). The error on the Cl/B ratio is of the order of 15%, calculated from the accuracy on standard measurements. The symbols for each textural domain are reported in the legend and the colours are different for every sample.

5.4. Serpentinisation stages in Iberia versus Newfoundland margin samples

Iberia samples S008 and S012 have distinct textural sites of serpentine with mesh rim, mesh centres and bastite (with prominently zoned bastite in major and trace elements for S012). The serpentine textures after the precursor minerals are confirmed by distinct transition metal compositions with a rather constant Ni/Cr (Fig. 4) for the olivine and orthopyroxene sites. Variable loss of Zn, Mn, and Co is observed and can be explained by loss of the elements to the fluid, or the uptake into another phase (e.g., magnetite and sulphides, see Section 5.1.).

Limited variations in $\delta^{18}O$ for the mesh rims of both S008 and S012 (Fig. 6, Table S5) are correlated with a slight increase in Cl/B (scenario (ii), Fig. 9D, E), suggesting that the fluid became more saline at a relatively constant serpentinisation temperature (Table 1). The same trend is visible for the mesh centres and bastite of S008, with higher Cl/B for the latter (Fig. 9D). On the other hand, the mesh centres and bastite of S012 show greater variability in the oxygen isotope composition, with constant Cl/B of ~10–15 (scenario (i), Fig. 9E). This feature is in line with a constant fluid composition and a range in $\delta^{18}O_{serpentine}$ due to temperature variations. Sample S012 from Iberia is a relevant example where the textural sequence of serpentinisation corresponds to a clear temperature trend. Fig. 10 shows the correlation between the oxygen isotopic composition of the serpentine and the temperature (calculated using the fractionation factor of Vho et al., 2019) for the distinct textures of sample S012 (Iberia). Given that the oxygen isotopic composition of the fluid may progressively evolve towards a heavier composition during closed-system serpentinisation, the temperature calculation can be performed for different oxygen isotope compositions of the fluid. Realistic values are those obtained using a fluid composition between that of seawater ($\delta^{18}O_{fluid}$ = 0‰, preferred scenario based on Cl/B considerations) and the most evolved seawater-derived fluid so far sampled in a natural environment ($\delta^{18}O_{fluid}$ = 2.4‰; Snake Pit vent field, Mid-Atlantic Ridge at Kane site 23°22′N, Campbell et al., 1988). The increase in the oxygen isotopic composition of the serpentine for the sequential textures describes a decrease in temperature from the onset of the serpentinisation at the mesh rims (~200 °C) to bastite A (150 °C) and down to 60–65 °C for bastite B and bastite C (Fig. 10). The temperature calculation was made for a seawater-fluid composition ($\delta^{18}O$ = 0‰, Table 1). The calculation would result in higher temperature of serpentinisation if a higher $\delta^{18}O$ fluid composition is considered (hydrothermally altered fluid; Fig. 10).

Sample S008 displays limited variability in the O isotope composition between the textural sites, corresponding to a serpentinisation temperature starting at ~180 °C for the mesh rim (assuming $\delta^{18}O_{fluid}$ = 0‰), and ending at 140 °C for both the mesh centre and the bastite (Fig. 11). These temperature estimates represent a lower limit and would be higher if a more evolved fluid with $\delta^{18}O_{fluid}$ > 0‰ were considered. These calculated temperatures are in agreement with previously published data using coupled serpentine-magnetite oxygen isotope thermometry that yielded temperatures of 150–120 °C (±50 °C) according to the fractionation factor of Wenner and Taylor (1971) (Agrinier et al., 1996; Plas, 1997). At the depth of our samples in Site 1070, Skelton and Valley (2000) measured a serpentine oxygen isotopic composition of 5.0‰, represented by a dashed-line in Fig. 6. While this value homogenises the whole rock composition, the results of our study

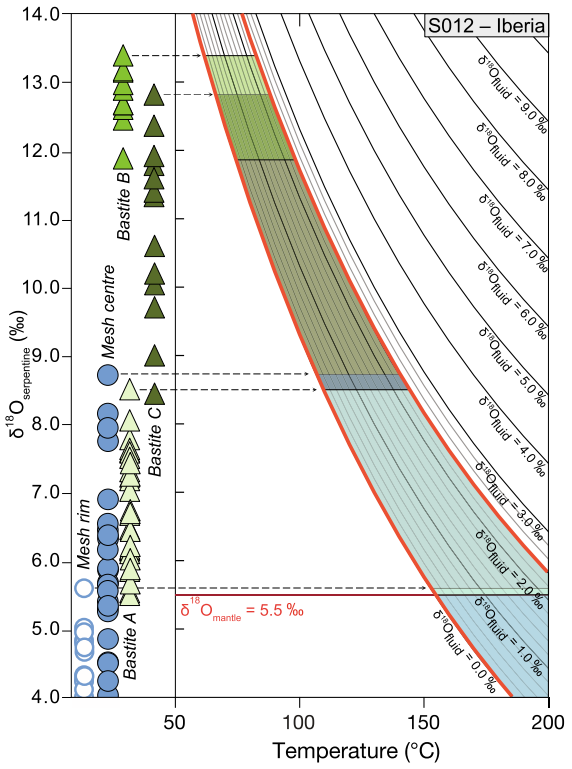

Fig. 10. Serpentinisation temperatures calculated from measured oxygen isotope compositions of texturally distinct serpentine (sample S012, Iberia) using the fractionation factor of Vho et al. (2019). The curves correspond to the O isotopic composition of the serpentinising fluid. The two red curves represent the O isotope signature of seawater and of the evolved seawaterderived fluid (Campbell et al., 1988). The coloured zones delimit the temperature and fluid composition conditions that produce the O isotope signature of serpentine. The δ18O composition of serpentine increases, consistent with the textural sequence of serpentinisation (mesh rim, mesh centre and bastite). This is interpreted as a temperature decrease during serpentinisation.

Table 1
$\delta^{18}O$ compositions of serpentine for the different textures of the four samples, their calculated temperatures using the fractionation factor of Vho et al. (2019) and assuming $\delta^{18}O_{fluid}$ = 0‰.

Sample	Locality	Textural position	$\delta^{18}O$ (‰)	Temperature (°C) Vho et al. (2019)	Temperature (°C) Zheng (1993)
S006	Newfoundland	Mesh	7.1–8.2	130–110	120–110
		Bastite	5.7–7.7	150–120	140–120
		Vein	6.8–7.4	130–120	125–120
S007	Newfoundland	Mesh	6.3–8.4	140–110	135–105
		Bastite	7.3–9.3	125–100	120–95
S008	Iberia	Mesh rim	3.7–4.9	190–165	180–155
		Mesh centre	3.7–6.3	190–140	180–135
		Bastite	3.3–6.1	200–145	190–135
		Vein	4.2–4.9	180–165	170–155
S012	Iberia	Mesh rim	3.9–6.1	185–145	175–135
		Mesh centre	4.0–8.7	185–105	170–100
		Bastite A	5.5–8.5	150–110	145–105
		Bastite B	12.0–13.5	70–60	70–60
		Bastite C	8.5–12.9	110–65	105–65

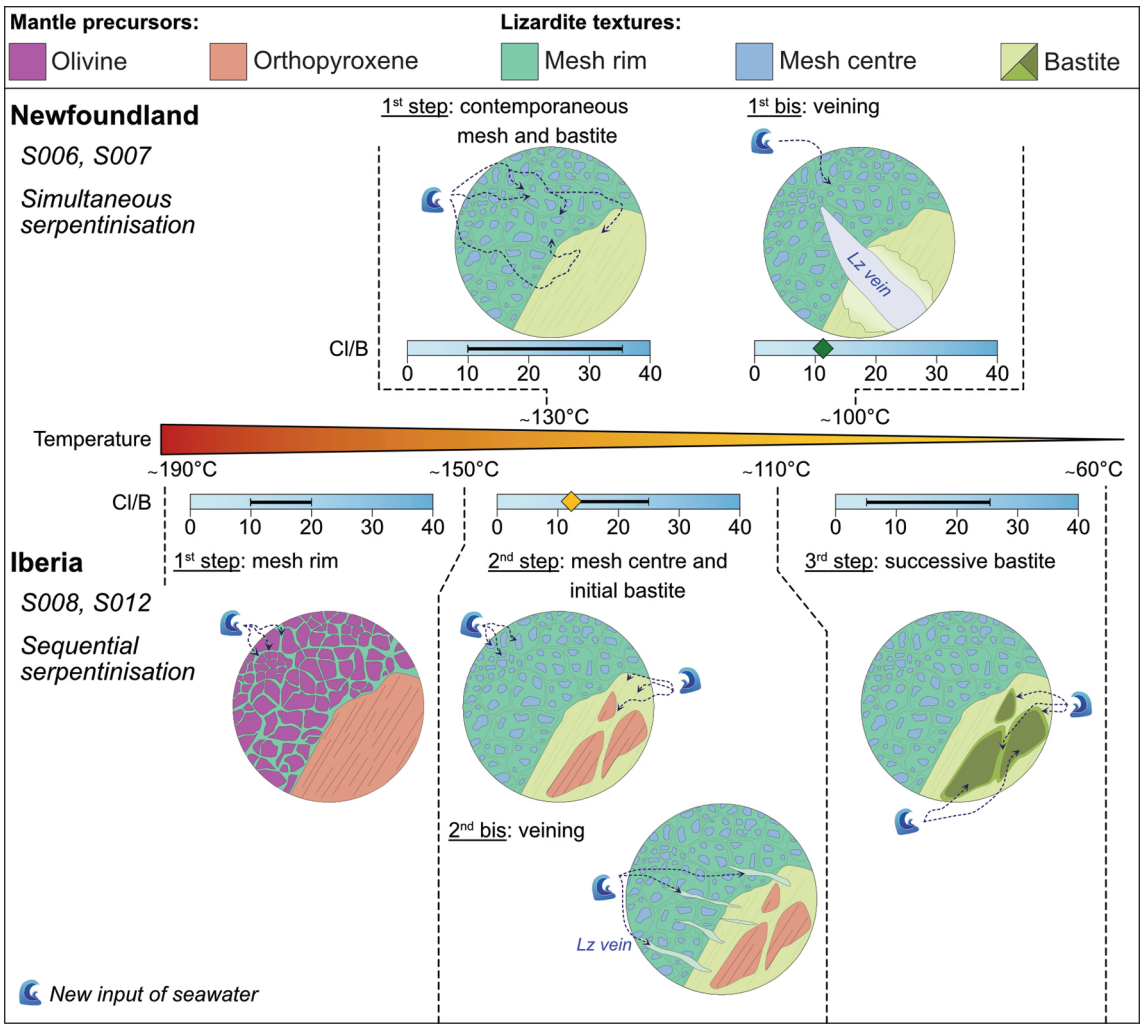

Fig. 11. Schematic illustration representing the similarities and differences between the cases of simultaneous (Newfoundland) and sequential (Iberia) serpentinisation. The successive steps for Iberia are associated with a decrease in temperature and a successive input of seawater that in case of the bastite evolves in a near-closed system as monitored by evolving Cl/B ratios. The coloured diamonds in the Cl/B range refer to the vein compositions (yellow: S006, Newfoundland; green: S008, Iberia), while the black bands mark the Cl/B compositions of the corresponding step. The wave symbol represents the successive input of seawater in the system and emphasises the multistage nature of the serpentinisation reactions.

help to recognise complex oxygen isotopic heterogeneity ranging from 3.9‰ to 13.5‰ in sample S012. This demonstrates that oxygen isotopic complexity cannot be properly resolved by bulk and/or mineral separates.

Newfoundland samples S006 and S007 contain serpentinites with clear textural sites after primary minerals olivine and orthopyroxene. Their textural distinctions have been confirmed by major and trace element compositions, the bastite being enriched in Al and Cr while the mesh contains more Ni. Chemical exchange between mesh and bastite sites during serpentinisation is indicated by the redistribution of Al and transition metals with significant variations in Ni/Cr (Fig. 4, columns 1 and 2). This feature is mirrored by a similar SiO_2 composition between the mesh and bastite of Newfoundland samples S006 and S007 (Fig. 2B, Table S3). The lowest Cl/B ratio in both Newfoundland samples is ~10–15 and increases up to 35 in the mesh and in the bastite of S007, at constant $\delta^{18}O_{serpentine}$ (Fig. 9C). The same evolution is observed in the mesh of S006, corresponding to scenario (ii) above, where Cl is passively enriched in the fluid at constant T (Fig. 9B). Mesh of S007 corresponds to scenario (iii) where Cl/B increases along with $\delta^{18}O_{serpentine}$. In this case, the influence of variations in temperature and/or fluid composition cannot be resolved. All textures of both samples have the same range in O isotope composition. For all textures of S006 and S007, the temperature can be calculated from the $\delta^{18}O_{serpentine}$ corresponding to the lowest Cl/B value, which is taken to best indicate serpentinisation by a fluid least equilibrated with rock, i.e., seawater with $\delta^{18}O = 0‰$. The calculated temperatures are between 100 and 150 °C and give the lower temperature limit for serpentinisation at the Newfoundland passive margin.

Two types of veins are present in the samples: the cross-cutting vein in S006, which has a different chemistry to the host-rock, and the infiltrating veinlets in S008, which retain the chemical signature of the protolith. In S006, the vein formation affects the former serpentine texture by changing the major and trace element concentrations of the bastite close to the vein. The $\delta^{18}O$ composition of the vein is homogeneous and similar to the oxygen isotopic signature of the bastite. This suggests that the vein formed during or shortly after the serpentinisation of the mantle orthopyroxene at a similar temperature, in a fluid-dominated environment. On the other hand, veinlets in S008 are interpreted to overprint former serpentine textures (bastite and mesh) while maintaining their local chemical signatures. The $\delta^{18}O$ composition of the veinlets is comparable to that of the bastite and the mesh, suggesting a coeval infiltration at a similar temperature.

These results suggest that S012 (Iberia) was serpentinised at lower temperature than S008 (Iberia), and that both Iberian samples

experienced warmer serpentinisation temperatures than the Newfoundland samples, at least for the first serpentinisation stage, i.e., mesh rim and centre (Fig. 11). Finally, we propose that the serpentinisation of mantle peridotites from the Iberia margin was sequential. It started at a higher temperature than in Newfoundland margin and experienced distinct episodes of hydration without element redistribution between the textural sites. The final stage of serpentinisation occurred at a low temperature of 60 °C. The large temperature drop during serpentinisation of the Iberian samples can be reconciled with progressive mantle exhumation bringing ultramafic rocks to shallower depths. Serpentinisation of the mantle peridotites in the Newfoundland margin occurred at a rather low temperature (100–150 °C) during a coeval event with simultaneous hydration of olivine and orthopyroxene (Fig. 11) with a seawater-derived fluid that evolved to a more saline fluid. The overall lower temperature can be explained by hydration of the mantle peridotites at shallower depths.

5.5. Implications for the deep biosphere

Of all the metabolic reactions that provide material and energy for life, the tri-carboxylic acid (TCA) cycle is considered the most important driver of energy catabolism in cells (e.g., Brovarone et al., 2020). The acetyl-coenzyme A (acetyl-CoA) pathway, which is considered to be the oldest carbon fixation process (e.g., Sojo et al., 2016), helps metabolic substrates such as sugars, lipids and amino acids to enter the TCA cycle, starting with the reduction of CO_2. In the acetyl-CoA pathway, organic compounds and phosphate are synthesised by a group of proteins that require an H^+ gradient (pH gradient) across the plasma membrane. Thereby, hydrogen is one of the main substrates of the carbon fixation pathway. Moreover, transition metals and metal sulphides (such as Fe-Ni sulphides) have the ability to catalyse organic reactions (Russell et al., 2010, and references therein). Samples from both Newfoundland and Iberia have low magnetite abundances, but this parameter has been shown not to be critical for H_2 production during serpentinisation, as it can also be associated with the crystallisation of ferric serpentine (Klein et al., 2014). Recent studies have further highlighted the significant H_2 and CH_4 production at ocean-continent transition (Liu et al., 2023).

Our study reconstructs the changing conditions of serpentinisation in the two settings (temperature and fluid salinity evolution). Samples from Newfoundland underwent simultaneous serpentinisation of olivine and orthopyroxene with chemical exchange of major, minor and trace elements over a narrow temperature range. On the other hand, samples from the Iberian margin probably underwent sequential hydration from olivine to orthopyroxene, starting in a warmer environment, possibly deeper in the lithosphere, over a wider temperature range and cooling to lower temperatures than in the Newfoundland passive margin. These reconstructed scenarios suggest that a concentrated amount of H_2 was produced relatively quickly in Newfoundland, compared to a small but prolonged H_2 production in Iberia. We speculate that the latter scenario is more likely to support microbial activity during the low-temperature stage of serpentinisation, when temperatures were suitable for life (below 120 °C; Kashefi and Lovley, 2003). Indeed, microbial activity has been detected in the Iberian margin serpentinites, where the estimated temperatures of the mixing zone between hydrothermal fluid and seawater are favourable for metabolic reactions (Klein et al., 2015). To our knowledge, no study on microbial activity associated with serpentinisation has been conducted at the Newfoundland passive margin. While these observations are made at the sample scale, an integrated H_2 production, until temperatures become too low to sustain microbial reactions, is to be expected when considering lithospheric scale of serpentinisation.

6. Conclusion

This study presents the first texturally controlled oxygen isotope study of serpentinites, reporting significant variations in *in situ* oxygen isotope composition and trace element chemistry at 10–100 μm scales. This combination allows to investigate the different parameters influencing the serpentinisation reaction (i.e., temperature, fluid composition, water–rock interaction). Transition metal concentration in serpentine is a robust marker for distinguishing the mantle precursors and also tracks potential chemical exchange between textural sites of serpentinisation. The Cl/B content of the serpentine is used as a proxy for the salinity of the serpentinising fluid, tracking the changing composition of the hydration fluid with progressive serpentinisation. The combination of these two geochemical signatures with the oxygen isotopic composition reveals simultaneous hydration of the mantle olivine and pyroxene in Newfoundland samples at temperatures of 100–130 °C. On the other hand, Iberian samples were likely serpentinised in sequential events at temperatures decreasing from ~190 to 60 °C. Our study highlights the power of *in situ* analysis to unravel the multistage history of serpentinisation and the parameters that influence serpentinisation reactions. This study may also shed light on the favourable environments for microbial activity in magma-poor passive margin settings.

Declaration of Competing Interest

The authors declare that they have no known competing financial interests or personal relationships that could have appeared to influence the work reported in this paper.

Data availability

Research data has been supplied via a repository: https://doi.org/10.17632/bkzck8np2g.1.

Acknowledgements

This study used samples provided by the Ocean Drilling Program, sponsored by the funding agencies of the participating countries under the management of Joint Oceanographic Institutions (JOI), Inc. We thank Anne-Sophie Bouvier and the SwissSIMS team for their assistance on the SIMS facility at the University of Lausanne, and the Nancy Ion Probe team for their assistance at CRPG-CNRS. We thank Martin Wille and Sukalpa Chatterjee for their valuable help with sample preparation and data acquisition at the TIMS laboratory of the Institute of Geological Sciences, University of Bern. We are grateful to Jörg Hermann, Francesca Piccoli, Michelle Ulrich and Renée Tamblyn for many fruitful scientific discussions. The research project is funded by SNSF projects Nr. 191959 to DR and R'Equip project Nr. 170722 to DR and TP. We greatly appreciate the editorial handling by Frieder Klein and Jeffrey G. Catalano, and the insightful comments from Manuel Menzel and an anonymous reviewer, which helped to improve the quality of this manuscript.

Appendix A. Supplementary material

The supplementary material for this paper includes schematic logs of the ODP drill cores, macroscopic scans of the sample thin sections and Raman spectra for the serpentine characterization. The supplementary material also contains additional plots of Mg + Fe versus Si (apfu), Fe versus Al (apfu), all the X-ray maps and B versus U (μg g^{-1}) plot. A description of the sample locality and mineral assemblages is available for readers, and data tables of chemical analysis (major, minor, and trace elements, Sr isotopes and O isotopes) are also reported. Supplementary data to this article can be found online at https://doi.org/10.1016/j.gca.2023.06.032.

References

Abe, N., 2001. Petrochemistry of serpentinized peridotite from the Iberia Abyssal Plain (ODP Leg 173): its character intermediat between sub-oceanic and sub-continental upper mantle. Geol. Soc. London Spec. Publ. 187, 143–159.

Agrinier, P., Cannat, M., 1997. Oxygen-isotope constraints on serpentinization processes in ultramafic rocks from the Mid-Atlantic Ridge (23°N). Notes 153, 95.

Agrinier, P., Mevel, C., Girardeau, J., 1988. Hydrothermal alteration of the peridotites cored at the ocean/continent boundary of the Iberian margin: petrologic and stable isotope evidence. Proc. Ocean Drill. Program, Sci. Results 103.

Agrinier, P., Hékinian, R., Bideau, D., Javoy, M., 1995. O and H stable isotope compositions of oceanic crust and upper mantle rocks exposed in the Hess Deep near the Galapagos Triple Junction. Earth Planet. Sci. Lett. 136, 183–196.

Agrinier, P., Cornen, G., Beslier, M.-O., 1996. Mineralogical and oxygen isotopic features of serpentinites recovered from the ocean/continent transition in the Iberia Abyssal Plain. Proc. Ocean Drill. Program, 149 Sci Results 149, 541–552.

Albers, E., Kahl, W.A., Beyer, L., Bach, W., 2020. Variant across-forearc compositions of slab-fluids recorded by serpentinites: Implications on the mobilization of FMEs from an active subduction zone (Mariana forearc). Lithos 364, 105525.

Alt, J.C., Shanks, W.C., 1998. Sulfur in serpentinized oceanic peridotites: Serpentinization processes and microbial sulfate reduction. J. Geophys. Res. Solid Earth 103, 9917–9929.

Alt, J.C., Shanks, W.C., Bach, W., Paulick, H., Garrido, C.J., Beaudoin, G., 2007. Hydrothermal alteration and microbial sulfate reduction in peridotite and gabbro exposed by detachment faulting at the Mid-Atlantic Ridge, 15°20′N (ODP Leg 209): A sulfur and oxygen isotope study. Geochem. Geophys. Geosyst. 8.

Bach, W., Garrido, C.J., Paulick, H., Harvey, J., Rosner, M., 2004. Seawater-peridotite interactions: First insights from ODP Leg 209, MAR 15°N. Geochem. Geophys. Geosyst. 5.

Bach, W., Paulick, H., Garrido, C.J., Ildefonse, B., Meurer, W.P., Humphris, S.E., 2006. Unraveling the sequence of serpentinization reactions: Petrography, mineral chemistry, and petrophysics of serpentinites from MAR 15°N (ODP Leg 209, Site 1274). Geophys. Res. Lett. 33.

Barnes, J.D., Sharp, Z.D., 2006. A chlorine isotope study of DSDP/ODP serpentinized ultramafic rocks: Insights into the serpentinization process. Chem. Geol. 228, 246–265.

Barnes, J.D., Paulick, H., Sharp, Z.D., Bach, W., Beaudoin, G., 2009. Stable isotope (δ18O, δD, δ37Cl) evidence for multiple fluid histories in mid-Atlantic abyssal peridotites (ODP Leg 209). Lithos 110, 83–94.

Beard, J.S., Frost, B.R., Fryer, P., Mccaig, A., Searle, R., Ildefonse, B., Zinin, P., Sharma, S. K., 2009. Onset and progression of serpentinization and magnetite formation in olivine-rich troctolite from IODP Hole U1309D. J. Petrol. 50, 387–403.

Beard, J.S., Hopkinson, L., 2000. A fossil, serpentinization-related hydrothermal vent, Ocean Drilling Program Leg 173, Site 1068 (Iberia Abyssal Plain): Some aspects of mineral and fluid chemistry. J. Geophys. Res. Solid Earth 105, 16527–16539.

Ben, O.D., White, W.M., Patchett, J., 1989. The geochemistry of marine sediments, island arc magma genesis, and crust-mantle recycling. Earth Planet. Sci. Lett. 94, 1–21.

Beslier, M.O., Ask, M., Boillot, G., 1993. Ocean-continent boundary in the Iberia Abyssal Plain from multichannel seismic data. Tectonophysics 218, 383–393.

Bowen, N.L., Tuttle, O.F., 1949. The system MgO-SiO2-H2O. Bull. Geol. Soc. Am. 60, 439–460.

Brovarone, A.V., Butch, C.J., Ciappa, A., Cleaves, H.J., Elmaleh, A., Faccenda, M., Feineman, M., Hermann, J., Nestola, F., Cordone, A., Giovannelli, D., 2020. Let there be water: How hydration/dehydration reactions accompany key Earth and life processes. Am. Mineral. 105, 1152–1160.

Campbell, A.C., Palmer, M.R., Klinkhammer, G.P., Bowers, T.S., Edmond, J.M., Lawrence, J.R., Casey, J.F., Thompson, G., Humphris, S., Rona, P., Karson, J.A., 1988. Chemistry of hot springs on the Mid-Atlantic Ridge. Nature 335, 514–519.

Decitre, S., Deloule, E., Reisberg, L., James, R., Agrinier, P., Mével, C., 2002. Behavior of Li and its isotopes during serpentinization of oceanic peridotites. Geochem. Geophys. Geosyst. 3, 1–20.

Deschamps, F., Guillot, S., Godard, M., Chauvel, C., Andreani, M., Hattori, K., 2010. In situ characterization of serpentinites from forearc mantle wedges: Timing of serpentinization and behavior of fluid-mobile elements in subduction zones. Chem. Geol. 269, 262–277.

Deschamps, F., Guillot, S., Godard, M., Andreani, M., Hattori, K., 2011. Serpentinites act as sponges for fluid-mobile elements in abyssal and subduction zone environments. Terra Nov. 23, 171–178.

Deschamps, F., Godard, M., Guillot, S., Hattori, K., 2013. Geochemistry of subduction zone serpentinites: A review. Lithos 178, 96–127.

Eddy, M.P., Jagoutz, O., Ibañez-Mejia, M., 2017. Timing of initial seafloor spreading in the Newfoundland-Iberia rift. Geology 45, 527–530.

Eiler, J.M., Valley, J.W., Stolper, E.M., 1996. Oxygen isotope ratios in olivine from the Hawaii Scientific Drilling Project. J. Geophys. Res. 101, 11807–11813.

Elderfield, H., 1986. Strontium isotope stratigraphy. Palaeogeogr. Palaeoclimatol. Palaeoecol. 57, 71–90.

Evans, B.W., 2004. The serpentinite multisystem revisited: Chrysotile is metastable. Int. Geol. Rev. 46, 479–506.

Evans, B.W., 2008. Control of the products of serpentinization by the Fe2+ Mg-1 exchange potential of olivine and orthopyroxene. J. Petrol. 49, 1873–1887.

Francheteau, J., Armijo, R., Cheminée, J.L., Hekinian, R., Lonsdale, P., Blum, N., 1990. 1 Ma East Pacific Rise oceanic crust and uppermost mantle exposed by rifting in Hess Deep (equatorial Pacific Ocean). Earth Planet. Sci. Lett. 101, 281–295.

Frost, R.B., Beard, J.S., 2007. On silica activity and serpentinization. J. Petrol. 48, 1351–1368.

Früh-Green, G.L., Plas, A., Lécuyer, C., 1996. Petrologic and stable isotope constraints on hydrothermal alteration and serpentinization of the EPR shallow mantle at Hess Deep (Site 895). Proc. Ocean Drill. Program Sci. Results 147, 255–291.

Hansen, C.T., Meixner, A., Kasemann, S.A., Bach, W., 2017. New insight on Li and B isotope fractionation during serpentinization derived from batch reaction investigations. Geochem. Cosmochim. Acta 217, 51–79.

Hébert, R., Gueddari, K., Laflèche, M.R., Beslier, M.O., Gardien, V., 2001. Petrology and geochemistry of exhumed peridotites and gabbros at non-volcanic margins: ODP Leg 173 West Iberia ocean-continent transition zone. Geol. Soc. Spec. Publ. 187, 161–189.

Hess, J., Bender, M.L., Schilling, J.G., 1986. Evolution of the ratio of strontium-87 to strontium-86 in seawater from Cretaceous to present. Science 231, 979–984.

Jones, C.E., Jenkyns, H.C., Coe, A.L., Stephen, H.P., 1994. Strontium isotopic variations in Jurassic and Cretaceous seawater. Geochim. Cosmochim. Acta 58, 3061–3074.

Kahl, W.A., Jöns, N., Bach, W., Klein, F., Alt, J.C., 2015. Ultramafic clasts from the South Chamorro serpentine mud volcano reveal a polyphase serpentinization history of the Mariana forearc mantle. Lithos 227, 1–20.

Kashefi, K., Lovley, D.R., 2003. Extending the upper temperature limit for life. Science 301, 934.

Kendrick, M.A., Honda, M., Pettke, T., Scambelluri, M., Phillips, D., Giuliani, A., 2013. Subduction zone fluxes of halogens and noble gases in seafloor and forearc serpentinites. Earth Planet. Sci. Lett. 365, 86–96.

Klein, F., Bach, W., McCollom, T.M., 2013. Compositional controls on hydrogen generation during serpentinization of ultramafic rocks. Lithos 178, 55–69.

Klein, F., Bach, W., Humphris, S.E., Kahl, W.A., Jöns, N., Moskowitz, B., Berquó, T.S., 2014. Magnetite in seafloor serpentinite-Some like it hot. Geology 42, 135–138.

Klein, F., Humphris, S.E., Guo, W., Schubotz, F., Schwarzenbach, E.M., Orsi, W.D., 2015. Fluid mixing and the deep biosphere of a fossil Lost City-type hydrothermal system at the Iberia Margin. Proc. Natl. Acad. Sci. 112, 12036–12041.

Klein, F., Humphris, S.E., Bach, W., 2020. Brucite formation and dissolution in oceanic serpentinite. Geochem. Perspect. Lett. 16, 1–5.

Klein, F., Le Roux, V., 2020. Quantifying the volume increase and chemical exchange during serpentinization. Geology 48, 552–556.

Kodolányi, J., Pettke, T., 2011. Loss of trace elements from serpentinites during fluid-assisted transformation of chrysotile to antigorite - An example from Guatemala. Chem. Geol. 284, 351–362.

Kodolányi, J., Pettke, T., Spandler, C., Kamber, B.S., Ling, K.G., 2012. Geochemistry of ocean floor and fore-arc serpentinites: Constraints on the ultramafic input to subduction zones. J. Petrol. 53, 235–270.

Lanari, P., Vidal, O., De Andrade, V., Dubacq, B., Lewin, E., Grosch, E.G., Schwartz, S., 2014. XMapTools: A MATLAB©-based program for electron microprobe X-ray image processing and geothermobarometry. Comput. Geosci. 62, 227–240.

Lanari, P., Vho, A., Bovay, T., Airaghi, L., Centrella, S., 2019. Quantitative compositional mapping of mineral phases by electron probe micro-analyser. Geol. Soc. London Spec. Publ. 478, 39–63.

Liu, Z., Perez-Gussinye, M., García-Pintado, J., Mezri, L., Bach, W., 2023. Mantle serpentinization and associated hydrogen flux at North Atlantic magma-poor rifted margins. Geology 51, 284–289.

Martin, B., Fyfe, W.S., 1970. Some experimental and theoretical observations on the kinetics of hydration reactions with particular reference to serpentinization. Chem. Geol. 6, 185–202.

Mattey, D., Lowry, D., Macpherson, C., 1994. Oxygen isotope composition of mantle peridotite. Earth Planet. Sci. Lett. 128, 231–241.

McCulloch, M.T., Gregory, R.T., Wasserburg, G.J., Taylor, H.P., 1981. Sm-Nd, Rb-Sr, and 180/160 isotopic systematics in an oceanic crustal section: Evidence from the Samail Ophiolite. J. Geophys. Res. 86, 2721–2735.

McDonough, W.F., Sun s, S., 1995. The composition of the Earth. Chem. Geol. 120, 223–253.

Mevel, C., Stamoudi, C., 1996. Hydrothermal Alteration of the Upper-Mantle Section at Hess Deep. Proc. Ocean Drill. Program, 147 Sci. Results 147.

Niu, Y., 2004. Bulk-rock major and trace element compositions of abyssal peridotites: Implications for mantle melting, melt extraction and post-melting processes beneath mid-ocean ridges. J. Petrol. 45, 2423–2458.

Oyanagi, R., Okamoto, A., Harigane, Y., Tsuchiya, N., 2018. Al-zoning of serpentine aggregates in mesh texture induced by metasomatic replacement reactions. J. Petrol. 59, 613–634.

Paulick, H., Bach, W., Godard, M., De Hoog, J.C.M., Suhr, G., Harvey, J., 2006. Geochemistry of abyssal peridotites (Mid-Atlantic Ridge, 15°20′N, ODP Leg 209): Implications for fluid/rock interaction in slow spreading environments. Chem. Geol. 234, 179–210.

Péron-Pinvidic, G., Manatschal, G., 2009. The final rifting evolution at deep magma-poor passive margins from Iberia-Newfoundland: a new point of view. Int. J. Earth Sci. 98, 1581–1597.

Peters, D., Bretscher, A., John, T., Scambelluri, M., Pettke, T., 2017. Fluid-mobile elements in serpentinites: Constraints on serpentinisation environments and element cycling in subduction zones. Chem. Geol. 466, 654–666.

Peters, D., Pettke, T., 2017. Evaluation of major to ultra trace element bulk rock chemical analysis of nanoparticulate pressed powder pellets by LA-ICP-MS. Geostand. Geoanal. Res. 41, 5–28.

Pettke, T., Oberli, F., Audétat, A., Guillong, M., Simon, A.C., Hanley, J.J., Klemm, L.M., 2012. Recent developments in element concentration and isotope ratio analysis of individual fluid inclusions by laser ablation single and multiple collector ICP-MS. Ore Geol. Rev. 44, 10–38.

Plas, A., 1997. Petrologic and stable isotope constraints on fluid-rock interaction, serpentinization and alternation of oceanic ultramafic rocks. University of Zürich.

Prichard, H.M., 1979. A petrographie study of the process of serpentinisation in ophiolites and the ocean crust. Contrib. Mineral. Petrol. 68, 231–241.
Rampone, E., Bottazzi, P., Ottolini, L., 1991. Complementary Ti and Zr anomalies in orthopyroxene and clinopyroxene from mantle peridotites. Nature 354, 518–520.
Reid, I.D., 1994. Crustal structure of a nonvolcanic rifted margin east of Newfoundland. J. Geophys. Res. 99, 15161–15180.
Robertson, A.H.F., 2007. Evidence of continental breakup from the Newfoundland rifted margin (Ocean Drilling Program Leg 210): Lower cretaceous seafloor formed by exhumation of subcontinental mantle lithosphere and the transition to seafloor spreading. In: Proceedings of the Ocean Drilling Program: Scientific Results, pp. 1–69.
Rouméjon, S., Cannat, M., Agrinier, P., Godard, M., Andreani, M., 2015. Serpentinization and fluid pathways in tectonically exhumed peridotites from the southwest Indian ridge (62–65°E). J. Petrol. 56, 703–734.
Rouméjon, S., Früh-Green, G.L., Orcutt, B.N., Party, I.E., 357 s., 2018. Alteration heterogeneities in peridotites exhumed on the southern wall of the Atlantis Massif (IODP Expedition 357). J. Petrol. 59, 1329–1358.
Rouméjon, S., Andreani, M., Früh-Green, G.L., 2019. Antigorite crystallization during oceanic retrograde serpentinization of abyssal peridotites. Contrib. Mineral. Petrol. 174, 1–25.
Russell, M.J., Hall, A.J., Martin, W., 2010. Serpentinization as a source of energy at the origin of life. Geobiology 8, 355–371.
Saccocia, P.J., Seewald, J.S., Shanks, W.C., 2009. Oxygen and hydrogen isotope fractionation in serpentine-water and talc-water systems from 250 to 450 °C, 50 MPa. Geochim. Cosmochim. Acta 73, 6789–6804.
Sanfilippo, A., Tribuzio, R., Tiepolo, M., 2014. Mantle-crust interactions in the oceanic lithosphere: Constraints from minor and trace elements in olivine. Geochim. Cosmochim. Acta 141, 423–439.
Scambelluri, M., Müntener, O., Hermann, J., Piccardo, G.B., Trommsdorff, V., 1995. Subduction of water into the mantle: History of an Alpine peridotite. Geology 23, 459–462.
Scambelluri, M., Rampone, E., Piccardo, G.B., 2001. Fluid and element cycling in subducted serpentinite: A trace-element study of the Erro-Tobbio high-pressure ultramafites (Western Alps, NW Italy). J. Petrol. 42, 55–67.
Scambelluri, M., Müntener, O., Ottolini, L., Pettke, T.T., Vannucci, R., 2004. The fate of B, Cl and Li in the subducted oceanic mantle and in the antigorite breakdown fluids. Earth Planet. Sci. Lett. 222, 217–234.
Schwarzenbach, E.M., Früh-Green, G.L., Bernasconi, S.M., Alt, J.C., Plas, A., 2013. Serpentinization and carbon sequestration: A study of two ancient peridotite-hosted hydrothermal systems. Chem. Geol. 351, 115–133.
Scicchitano, M.R., Rubatto, D., Hermann, J., Shen, T., Padrón-Navarta, J.A., Williams, I. S., Zheng, Y.F., 2018. In Situ oxygen isotope determination in serpentine minerals by ion microprobe: Reference materials and applications to ultrahigh-pressure serpentinites. Geostand. Geoanal. Res. 42, 459–479.
Scicchitano, M.R., Spicuzza, M.J., Ellison, E.T., Tuschel, D., Templeton, A.S., Valley, J. W., 2021. In situ oxygen isotope determination in serpentine minerals by SIMS: Addressing matrix effects and providing new insights on serpentinisation at Hole BA1B (Samail ophiolite, Oman). Geostand. Geoanal. Res. 45, 161–187.
Seo, J.H., Guillong, M., Aerts, M., Zajacz, Z., Heinrich, C.A., 2011. Microanalysis of S, Cl, and Br in fluid inclusions by LA-ICP-MS. Chem. Geol. 284, 35–44.
Seyfried, W.E., Dibble, W.E., 1980. Seawater-peridotite interaction at 300°C and 500 bars: implications for the origin of oceanic serpentinites. Geochim. Cosmochim. Acta 44, 309–321.
Sharp, Z.D., Barnes, J.D., 2004. Water-soluble chlorides in massive seafloor serpentinites: a source of chloride in subduction zones. Earth Planet. Sci. Lett. 226, 243–254.
Shillington, D.J., Holbrook, W.S., Van Avendonk, H.J.A., Tucholke, B.E., Hopper, J.R., Louden, K.E., Larsen, H.C., Nunes, G.T., 2006. Evidence for asymmetric nonvolcanic rifting and slow incipient oceanic accretion from seismic reflection data ofnthe Newfoudland margin. J. Geophys. Res. Solid Earth 111.
Skelton, A.D.L., Valley, J.W., 2000. The relative timing of serpentinisation and mantle exhumation at the ocean-continent transition, Iberia: Constraints from oxygen isotopes. Earth Planet. Sci. Lett. 178, 327–338.
Sojo, V., Herschy, B., Whicher, A., Camprubí, E., Lane, N., 2016. The origin of life in alkaline hydrothermal vents. Astrobiology 16, 181–197.
Taylor, H.P., 1977. Water/rock interactions and the origin of H2O in granitic batholiths. J. Geol. Soc. London 133, 509–558.
Tucholke, B.E., Sibuet, J., Klaus, A., Arnaboldi, M., Delius, H., Engstrom, A.V., Galbrun, B., Gardin, S., Hiscott, R.N., Karner, G.D., Ladner, B.C., Leckie, R.M., Lee, C.-S., Manatschal, G., Marsaglia, K.M., Pletsch, T.K., Pross, J., Robertson, A.H.F., Sawyer, D.S., Sawyer, D.E., Shillington, D.J., Shirai, M., Shryane, T., Stant, S.A., Takata, H., Urquhart, E., Wilson, C., Zhao, X., 2004. Site 1277. Proc. Ocean Drill. Program, Part A Initial Reports 210, 39p.
Tutolo, B.M., Mildner, D.F.R., Gagnon, C.V.L., Saar, M.O., Seyfried, W.E., 2016. Nanoscale constraints on porosity generation and fluid flow during serpentinization. Geology 44, 103–106.
Uppström, L.R., 1974. The boron/chlorinity ratio of deep-sea water from the Pacific Ocean. Deep. Res. 21, 161–162.
Vho, A., Lanari, P., Rubatto, D., 2019. An internally-consistent database for oxygen isotope fractionation between minerals. J. Petrol. 60, 2101–2129.
Vils, F., Pelletier, L., Kalt, A., Müntener, O., Ludwig, T., 2008. The Lithium, Boron and Beryllium content of serpentinized peridotites from ODP Leg 209 (Sites 1272A and 1274A): Implications for lithium and boron budgets of oceanic lithosphere. Geochim. Cosmochim. Acta 72, 5475–5504.
Weis, D., Kieffer, B., Maerschalk, C., Barling, J., De Jong, J., Williams, G.A., Hanano, D., Pretorius, W., Mattielli, N., Scoates, J.S., Goolaerts, A., Friedman, R.M., Mahoney, J. B., 2006. High-precision isotopic characterization of USGS reference materials by TIMS and MC-ICP-MS. Geochem. Geophys. Geosyst. 7.
Wenner, D.B., Taylor, H.P., 1971. Temperatures of serpentinization of ultramafic rocks based on O18/O16 fractionation between coexisting serpentine and magnetite. Contrib. Mineral. Petrol. 32, 165–185.
Wenner, D.B., Taylor, H.P., 1973. Oxygen and hydrogen isotope studies of the serpentinization of ultramafic rocks in oceanic environments and continental ophiolite complexes. Am. J. Sci. 273, 207–239.
Whitmarsh, R.B., Sawyer, D.S., 1996. The ocean/continent transition beneath the Iberia Abyssal Plain and continental-rifting to seafloor-spreading processes. In: Proceedings-ocean Drilling Program Scientific Results, pp. 713–736.
Whitmarsh, R.B., Beslier, M.-O., Wallace, P.J., Abe, N., Basile, C., Beard, J.S., Froitzheim, N., Gardien, V., Hébert, R., Hopkinson, L.J., Kudless, K.E., Louvel, V., Manatschal, G., Newton, A.C., Rubenach, M.J., Skelton, A.D.L., Smith, S.E., Takayama, H., Tompkins, M.J., Turrin, B.D., Urquhart, E., Wallrabe-Adams, H.-J., Wilkens, R.H., Wilson, R.C.L., Wise, S.W.J., Zhao, X., 1998. Site 1070. Proc. Ocean Drill Program, Part A Initial Rep. 173, 265–294.
Whitney, D.L., Evans, B.W., 2010. Abbreviations for names of rock forming minerals. Mineral 95 (1), 185–187.
Xing, Y., Brugger, J., Scheuermann, P., Tan, C., Ji, S., Seyfried, W.E., 2022. An experimental and thermodynamic study of sphalerite solubility in chloride-bearing fluids at 300–450 °C, 500 bar: implications for zinc transport in seafloor hydrothermal systems. Geochim. Cosmochim. Acta 330, 131–147.
Zheng, Y.F., 1993. Calculation of oxygen isotope fractionation in hydroxyl-bearing silicates. Earth Planet. Sci. Lett. 120, 247–263.